Regular Article

Electronic structure and correlations of vitamin B_{12} studied within the Haldane-Anderson impurity model

Zafer Kandemir[1,2], Selma Mayda[1,2], and Nejat Bulut[1,a]

[1] Department of Physics, Izmir Institute of Technology, 35430 Urla, Turkey
[2] Department of Materials Science and Engineering, Izmir Institute of Technology, 35430 Urla, Turkey

Abstract. We study the electronic structure and correlations of vitamin B_{12} (cyanocobalamine) by using the framework of the multi-orbital single-impurity Haldane-Anderson model of a transition-metal impurity in a semiconductor host. The parameters of the effective Haldane-Anderson model are obtained within the Hartree-Fock (HF) approximation. The quantum Monte Carlo (QMC) technique is then used to calculate the one-electron and magnetic correlation functions of this effective model. We observe that new states form inside the semiconductor gap found by HF due to the intra-orbital Coulomb interaction at the impurity $3d$ orbitals. In particular, the lowest unoccupied states correspond to an impurity bound state, which consists of states from mainly the CN axial ligand and the corrin ring as well as the Co e_g-like orbitals. We also observe that the Co $(3d)$ orbitals can develop antiferromagnetic correlations with the surrounding atoms depending on the filling of the impurity bound states. In addition, we make comparisons of the HF+QMC data with the density functional theory calculations. We also discuss the photoabsorption spectrum of cyanocobalamine.

1 Introduction

1.1 Metalloproteins and metalloenzymes

Proteins are important building blocks of organisms. About one third of proteins have a metal atom such as iron, cobalt or zinc, and also about half of enzymes contain a metal atom [1–4]. The metal atom in these organometallic molecules is usually coordinated with nitrogen, oxygen or sulphur atoms. This kind of proteins and enzymes are called as metalloproteins and metalloenzymes. An example for metalloproteins is hemoglobin which contains iron, and is involved in the transportation of oxygen and carbon dioxide in blood. An example for metalloenzymes is vitamin B_{12}, which contains a cobalt atom and plays an important role in the production of red blood cells and in the functioning of the nervous system and the brain.

Metalloenzymes and metalloproteins form an unusual class of organometallic molecules with important catalytic functions; they enable various chemical reactions to take place in the biological environment of the organisms instead of requiring, for example, higher values for pressure or temperature. The mechanisms for the functioning of metalloenzymes and metalloproteins have been studied for more than half a century. However, much still remains to be understood about these organometallic molecules. In particular, we think that it is important to know whether

their unique chemical functions have a common underlying electronic mechanism.

As an example for metalloenzymes, in this paper we study the electronic structure of vitamin B_{12}, which is also called cobalamin (Cbl), by using the techniques of many-body physics. We have chosen to study Cbl because it contains relatively few atoms and is suitable for numerical calculations in addition to its biological importance. The molecular structure of Cbl was determined by X-ray measurements [5], and consists of a ligand and a nucleotide attached to a corrin ring as shown in Figure 1a. In the corrin ring, four nitrogen atoms are attached to the cobalt atom which is located at the center. Here, we concentrate on the cofactor cyanocobalamin (CNCbl) with the chemical formula $C_{63}H_{88}CoN_{14}O_{14}P$, in which a CN molecule is attached to Co as the axial ligand. The other two cofactors of Cbl are adenosylcobalamine (AdoCbl) and methylcobalamin (MeCbl), in which either an adenosyl or a methyl CH_3 group is attached to Co instead of CN as the axial ligand.

1.2 Comparison with the dilute magnetic semiconductors

The CNCbl exhibits an energy gap of about 2.2 eV in its electronic spectrum [6] and contains a transition metal atom. In this respect, it is similar to an entirely different class of compounds, the dilute magnetic semiconductors

ᵃ e-mail: nejatbulut@iyte.edu.tr
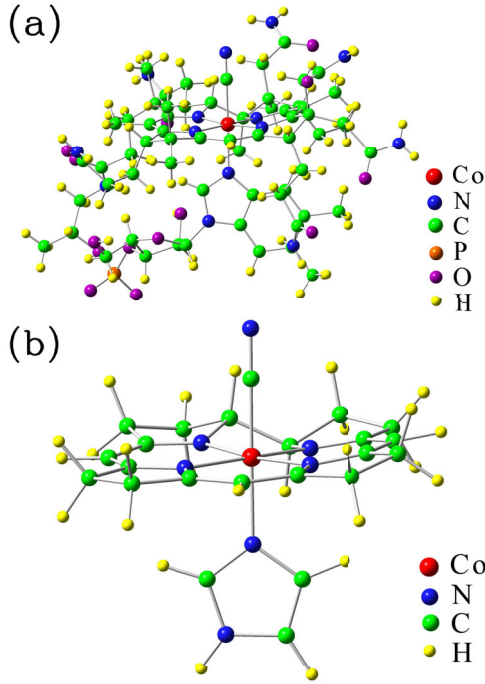
Fig. 1. (a) Schematic plot of the molecular structure of cyanocobalamine ($C_{63}H_{88}CoN_{14}O_{14}P$). (b) Schematic plot of the simpler truncated structure for cyanocobalamine, Im-[Co^{III}(corrin)]-CN^+, for which we perform numerical calculations.

(DMS) [7,8]. The DMS materials such as (Ga,Mn)As are obtained by substituting transition metal impurities into a semiconducting host material. They exhibit interesting physical properties such as long-range ferromagnetic correlations, which are found to exist between the Mn magnetic moments at elevated temperatures. The transport measurements have shown that, in the dilute limit, an impurity bound state exists near the top of the valence band in the semiconductor gap [9]. The impurity bound state, which is a sharp resonant state in the single-particle spectrum consisting of spectral weight from the Mn impurity and the host, plays a crucial role in determining the electronic and magnetic properties of (Ga,Mn)As [10–12] when studied within the framework of the Haldane-Anderson [13] model. For example, the long-range ferromagnetic correlations among the Mn impurities disappear rapidly as the impurity bound state becomes occupied with electrons.

1.3 Motivation

The comparison with the DMS materials leads naturally to the following questions: Do similar many-body effects play a role in determining the electronic and magnetic properties of CNCbl as well as the functioning of metalloenzymes and metalloproteins in general? What is the special role of the transition metal atom in the organometallic molecules? In metalloenzymes and metalloproteins, are there electronic states which are analogous

to the impurity bound state found in the DMS materials? If so, what role do they play in the catalytic functioning of these molecules? Is there a common underlying electronic mechanism for the functioning of the metalloproteins and metalloenzymes? The research presented in this paper is motivated mainly by these questions.

1.4 Haldane-Anderson model

As it was done previously for the DMS materials [10–12], in this paper we study the electronic structure and correlations of CNCbl by using the Haldane-Anderson model of a transition metal impurity in a semiconducting host. For this purpose, we first map the electronic structure of CNCbl onto the multi-orbital single-impurity Haldane-Anderson model by making use of the Hartree-Fock (HF) approximation. Then we study this effective Anderson Hamiltonian [14] by using QMC calculations with the Hirsch-Fye algorithm [15]. Hence, we study CNCbl by combining the HF and the QMC techniques, which is called as HF+QMC. There have been many previous studies of the electronic state of Cbl and other metalloproteins by using the density functional theory [16–27]. In contrast, here we study Cbl from the perspective of many-body physics within the framework of the Haldane-Anderson impurity model by using the HF+QMC approach.

The multi-orbital single-impurity Anderson Hamiltonian [14] is given by

$$
\begin{aligned}
H = &\sum_{m,\sigma}(\varepsilon_m - \mu)c^\dagger_{m\sigma}c_{m\sigma} + \sum_{\nu,\sigma}(\varepsilon_{d\nu} - \mu)d^\dagger_{\nu\sigma}d_{\nu\sigma} \\
&+ \sum_{m,\nu,\sigma}(V_{m\nu}c^\dagger_{m\sigma}d_{\nu\sigma} + V^*_{m\nu}d^\dagger_{\nu\sigma}c_{m\sigma}) \\
&+ \sum_\nu U_\nu n_{\nu\uparrow}n_{\nu\downarrow},
\end{aligned}
\tag{1}
$$

where $c^\dagger_{m\sigma}$ ($c_{m\sigma}$) creates (annihilates) an electron in host state m with spin σ, $d^\dagger_\nu$ (d_ν) is the creation (annihilation) operator for a localized electron at the Co ($3d_\nu$) orbital, and $n_{\nu\sigma} = d^\dagger_{\nu\sigma}d_{\nu\sigma}$. Here, ε_m and $\varepsilon_{d\nu}$ are the energies of the host and the $3d_\nu$ impurity states, respectively, $V_{m\nu}$ is the hybridization matrix element between these states and U_ν is the intra-orbital Coulomb repulsion. We have introduced a chemical potential μ since the QMC calculations are performed in the grand canonical ensemble.

This form of the Hamiltonian does not include the inter-orbital Coulomb interaction along with the Hund's coupling. In cobaltates, the Hund's coupling plays an important role [28], and we expect it to be important in Cbl also. In the present HF+QMC calculations the inter-orbital Coulomb correlations are taken into account only at the HF level, and not in the QMC calculations.

We note that the charge and spin states of Fe in hemoglobin were studied previously by using mean-field theory within the extended Haldane-Anderson model which contains the inter-orbital Coulomb interaction and the Hund's coupling [29]. In addition, the high-spin to low-spin transition due to oxygen binding in myglobin

was studied by using mean-field theory for the extended Haldane-Anderson model [30].

1.5 Truncated molecular structure for cyanocobalamine

We perform these calculations by using the simplified molecular structure Im-[Co^{III}(corrin)]-CN$^+$ shown in Figure 1b, as has been done in previous DFT calculations [24]. Here, it is clearly seen that Co is coordinated by 5 N and 1 C atoms, which forms an approximately octahedral configuration. In order to obtain this simplified structure, the nucleotide group attached to the corrin ring is truncated and the side chains of the corrin ring are replaced by hydrogen atoms. The resulting Im-[Co^{III}(corrin)]-CN$^+$ has 56 atoms, instead of 181 in CNCbl, and contains 238 electrons instead of 718. Our use of this truncated structure for modelling CNCbl decreases the number of the host eigenstates and the computational cost of the QMC calculations, because in the HF+QMC approach it is necessary to calculate all of the host Green's functions in order to determine the chemical potential as will be discussed below.

1.6 Outline of the paper

The outline of this paper is as follows. In Section 2, in order to obtain the one-electron parameters of the Anderson Hamiltonian, we perform Hartree-Fock calculations with the Gaussian program [31]. In particular, we first write the HF solution for the Fock matrix, which is defined in Section 2.1, in the orthogonal basis set of the natural atomic orbitals (NAO) [32,33]. From this, we obtain the one-electron parameters ε_m, $\varepsilon_{d\nu}$, and $V_{m\nu}$. The HF calculation finds an energy gap of 8.5 eV for the host electronic states. In addition, the hybridization matrix elements are largest between the Co e_g-like states and the atoms around Co, in particular, the CN axial ligand. For the intra-orbital Coulomb repulsion U_ν, we use the value obtained from the two-electron integrals. However, we also perform calculations for different values U_ν in order to see the dependence of the results. In the HF+QMC approach, the intra-orbital Coulomb repulsion is taken into account by both the HF and the QMC parts of the calculations. In order to eliminate this double-counting, the bare Co $(3d_\nu)$ energy levels $\varepsilon_{d\nu}$ are shifted by a constant amount.

In Section 3, we present QMC data on the single-particle and magnetic correlation functions for the effective Anderson Hamiltonian. We note that the QMC results on the electronic state and the magnetic correlations, and the resulting analysis presented in Section 3 are similar to the previous QMC study of the Haldane-Anderson model within the context of the DMS materials [11,12]. Here, in Section 3, the Hartree-Fock calculations find that the host eigenstates have a semiconducting gap in the energy interval -10.2 eV $\leq \varepsilon \leq -1.7$ eV. The HF+QMC results presented in Section 3 show that new single-particle states are induced in the intervals -10 eV $\lesssim \varepsilon \lesssim -8.5$ eV

and -5.5 eV $\lesssim \varepsilon \lesssim -2$ eV. We find that the states in the interval -10 eV $\lesssim \varepsilon \lesssim -8.5$ eV arise mainly from the doubly-occupied Co t_{2g}-like states, while containing smaller amount of states from the corrin ring. On the other hand, based on the QMC data on the single-particle and magnetic correlation functions, we conclude that the states in the interval -5.5 eV $\lesssim \varepsilon \lesssim -2$ eV represent impurity bound states arising from the strong hybridization of the Co e_g-like states with the host eigenstates from the valence band. These impurity bound states have sufficient spectral weight to accommodate 2 electrons including spin. Interestingly, only 0.4 of these electrons originate from the Co e_g-like orbitals, the remaining 1.6 electrons originate from the host states which consist of orbitals mainly from the CN axial ligand and to a lesser extent from the corrin ring. In Section 3, we also present QMC data on the magnetic correlation functions. We study the magnetic moment formation as a function of the electron filling, which is similar to the previous QMC studies on the DMS materials [11,12]. In addition, we show that magnetic moments develop in the valence-band host eigenstates which are strongly hybridized with the Co e_g-like orbitals. The size of these magnetic moments depend sensitively on the filling of the impurity bound states located at ≈ -5.5 eV and ≈ -4 eV. In addition, the magnetic moments of these host states are coupled antiferromagnetically to the Co e_g-like magnetic moments, and these correlations vanish rapidly with the electron filling of the impurity bound states. It is because of this filling dependence that we attribute the induced states at ≈ -5.5 eV and ≈ -4 eV to be arising from impurity bound states. It would be useful to experimentally look for signatures of the antiferromagnetic correlations which are predicted by the HF+QMC calculations. It would also be useful to look for experimental evidence that the states in the interval -5.5 eV $\lesssim \varepsilon \lesssim -2$ eV indeed arise from impurity bound states in CNCbl.

In Section 4, we present a discussion in which we compare the HF+QMC data with the DFT calculations on the same molecule. With respect to the HF results, the DFT calculations find that new single-particle spectral weight is induced in the intervals -10.5 eV $\leq \varepsilon \leq -8.0$ eV and -5.5 eV $\leq \varepsilon \leq -1.7$ eV. This is similar to the HF+QMC data. However, the overall distributions of the spectral weight obtained by the DFT and the HF+QMC calculations are very different. In the DFT calculations, the states in the interval -10.5 eV $\leq \varepsilon \leq -8.0$ eV do not arise from the upper-Hubbard states of the doubly-occupied Co t_{2g} orbitals. In addition, the states in the interval -5.5 eV $\leq \varepsilon \leq -1.7$ eV do not correspond to an impurity bound state. Furthermore, the magnetic correlations are absent in the DFT calculations. In Section 4, we also compare the HF+QMC data with the experimental data on the photoabsorption spectrum of CNCbl, which is characterized by several distinctive peaks. The HF+QMC data suggest that the lowest-energy excitations are dominated by the electron transfer from the Co t_{2g}-like states to the impurity bound states. In Section 4, we also discuss that the combined DFT+QMC technique may also be

applied to the same problem. In addition, we note that the inter-orbital Coulomb interaction with the Hund's coupling needs to be included in the QMC calculations before carrying out quantitative comparisons with the experimental data on CNCbl.

Section 5 gives the summary and conclusions of the paper.

2 Construction of the effective Anderson Hamiltonian

Various methods for the ab initio calculation of the parameters of the Anderson Hamiltonian had been developed for rare-earth, actinide and $3d$ compounds [34]. Here, we use the Hartree-Fock approximation to determine the parameters of the effective Haldane-Anderson model for the truncated molecule Im-[Co^{III}(corrin)]-CN$^+$.

In Section 2.1, we first define the Fock matrix and then discuss how the self-consistent Hartree-Fock solution for the Fock matrix is obtained. In Section 2.2, we introduce the natural atomic orbitals (NAO's) which form an orthogonal basis [32]. In Section 2.3, we use the Fock matrix written in the NAO basis to determine the bare energy levels and the hybridization parameters of the effective Haldane-Anderson model. In Section 2.4, we present results on the density of states obtained from the Hartree-Fock approximation. By mapping to the effective Haldane-Anderson model, the energies of the host states ε_m and the impurity levels $\varepsilon_{d\nu}$ are obtained. Here, we show the density of states of the host part of the model along with the positions of the bare Co $(3d_\nu)$ levels. The hybridization matrix elements obtained from the mapping to the Anderson Hamiltonian are presented in Section 2.5. In Section 2.6, we discuss the values of the onsite Coulomb repulsion used in the QMC simulations. In order to eliminate the effects of the double counting of the Coulomb interaction in HF+QMC, the Co $(3d_\nu)$ energy levels are shifted by μ_{DC}, which is discussed in Section 2.7. The results presented in Section 2 are based on reference [35].

At this point, it is necessary to discuss how the atomic coordinates of the molecule Im-[Co^{III}(corrin)]-CN$^+$, which are needed as input parameters for the Hartree-Fock calculations, are determined. Here, we use the approach taken by Kornobis et al. [24], which may be summarized as follows. X-ray measurements had been used to obtain with high accuracy the geometrical parameters for the molecule MeCbl [36]. In order to have an initial estimate of the atomic coordinates of CNCbl, the axial ligand CH$_3$ in MeCbl was replaced by CN. The resulting molecular structure for CNCbl was then truncated obtaining the simplified structure Im-[Co^{III}(corrin)]-CN$^+$. The final atomic coordinates were determined after performing an optimization on the coordinates of the simplified structure by using the DFT technique with the 6-31G(d) Gaussian basis set [31] and the BP86 exchange correlation functionals [37,38]. This way we obtain a reasonable set of values for the geometrical parameters, which are used as input in the Hartree-Fock calculations. The atomic coordinates

used in this paper for Im-[Co^{III}(corrin)]-CN$^+$ are the same as in reference [24].

2.1 Hartree-Fock solution and the Fock matrix

According to the electronic structure theory, the many-body wave function Ψ of the molecule is given by the Slater determinant of the one-electron molecular orbitals ψ_n. Within the Hartree-Fock mean-field approximation [39], the one-electron wave function $\psi_n(\mathbf{r})$ is determined from the self-consistent solution of

$$\left(-\frac{\hbar^2}{2m_e}\nabla_{\mathbf{r}}^2 + V_{ion}(\mathbf{r}) + \sum_m \int d^3 r' \frac{|\psi_m(\mathbf{r}')|^2}{|\mathbf{r}-\mathbf{r}'|} \right) \psi_n(\mathbf{r})$$
$$- \sum_m \int d^3 r' \frac{\psi_m^*(\mathbf{r}')\psi_n(\mathbf{r}')}{|\mathbf{r}-\mathbf{r}'|} \psi_m(\mathbf{r}) = E_n \psi_n(\mathbf{r}) \quad (2)$$

with E_n the molecular-orbital energy. Here, the left-hand side includes the kinetic-energy and the electron-ion potential $V_{ion}(\mathbf{r})$ terms in addition to the Hartree and the Fock contributions.

The molecular orbitals $|\psi_n\rangle$ can be expressed in terms of the N atomic orbitals $|\phi_i\rangle$,

$$|\psi_n\rangle = \sum_i^N C_{ni}|\phi_i\rangle, \quad (3)$$

where C_{ni} are the elements of the coefficient matrix $\mathbf{C}$. By substituting equation (3) into equation (2), the so-called Roothan equation is obtained [40],

$$\mathbf{C\,F} = \mathbf{E\,C\,S}. \quad (4)$$

Here, the overlap matrix $\mathbf{S}$ has the matrix elements $S_{ij} = \langle \phi_i | \phi_j \rangle$. Since the atomic orbitals $|\phi_i\rangle$ do not form an orthogonal basis, the overlap matrix is not diagonal. The matrix $\mathbf{E}$ is diagonal with the diagonal elements giving the molecular orbital energies, $E_{nm} = \delta_{nm}E_m$. The elements of the Fock matrix $\mathbf{F}$ are given by:

$$F_{ij} = \int d^3 r\, \phi_i^*(\mathbf{r}) \left(-\frac{\hbar^2}{2m_e}\nabla_{\mathbf{r}}^2 + V_{ion}(\mathbf{r}) \right) \phi_j(\mathbf{r})$$
$$+ \sum_{i',j'}^N D_{i'j'} \int d^3 r \int d^3 r' \frac{\phi_i^*(\mathbf{r})\phi_{i'}^*(\mathbf{r}')}{|\mathbf{r}-\mathbf{r}'|}$$
$$\times \left(\phi_j(\mathbf{r})\phi_{j'}(\mathbf{r}') - \phi_{j'}(\mathbf{r})\phi_j(\mathbf{r}') \right), \quad (5)$$

where

$$D_{ij} = \sum_n^{N_{el}} C_{ni}C_{nj} \quad (6)$$

forms the density matrix. Here, N_{el} denotes the total number of the electrons and also twice the number of the occupied molecular orbitals. For Im-[Co^{III}(corrin)]-CN$^+$, we have $N_{el} = 238$. Using as input the one- and two-electron integrals, the solution of the Roothan equation for E_n and the density matrix are obtained self-consistently

through iteration. In order to obtain the HF solution for Im-[Co^{III}(corrin)]-CN$^+$, we have used the Gaussian program [31] with the 6-31G basis set and $N = 347$ basis functions. We perform the HF calculations with the Gaussian 6-31G basis set instead of the 6-31G(d) set[1], which was used in the initial optimization, in order to increase the speed of the QMC calculations reported in Section 3. After the HF solution has been obtained, we have formed the Fock matrix. From the Fock matrix we have obtained the one-electron parameters of the effective Anderson Hamiltonian through a procedure outlined in the following two subsections.

2.2 Basis of the natural atomic orbitals

The overlap matrix $\mathbf{S}$ defined above is not diagonal, since the atomic orbitals do not form an orthogonal basis set. A convenient orthogonal basis for expressing $|\psi_n\rangle$ is provided by the basis of the natural atomic orbitals $|\tilde{\phi}_i\rangle$ [32]. The NAO's form a maximally localized basis set; they are similar to the atomic orbitals but they are also orthogonal. The NAO's are obtained by minimizing the function

$$\sum_i w_i \int d^3 r \, |\tilde{\phi}_i(\mathbf{r}) - \phi_i(\mathbf{r})|^2, \tag{7}$$

where w_i denotes the electron occupation number of the atomic orbital $|\phi_i\rangle$ obtained by the Hartree-Fock calculation. Here, we will first express the Fock matrix in the NAO basis, and from this deduce the parameters of the Anderson Hamiltonian except for the Coulomb repulsion.

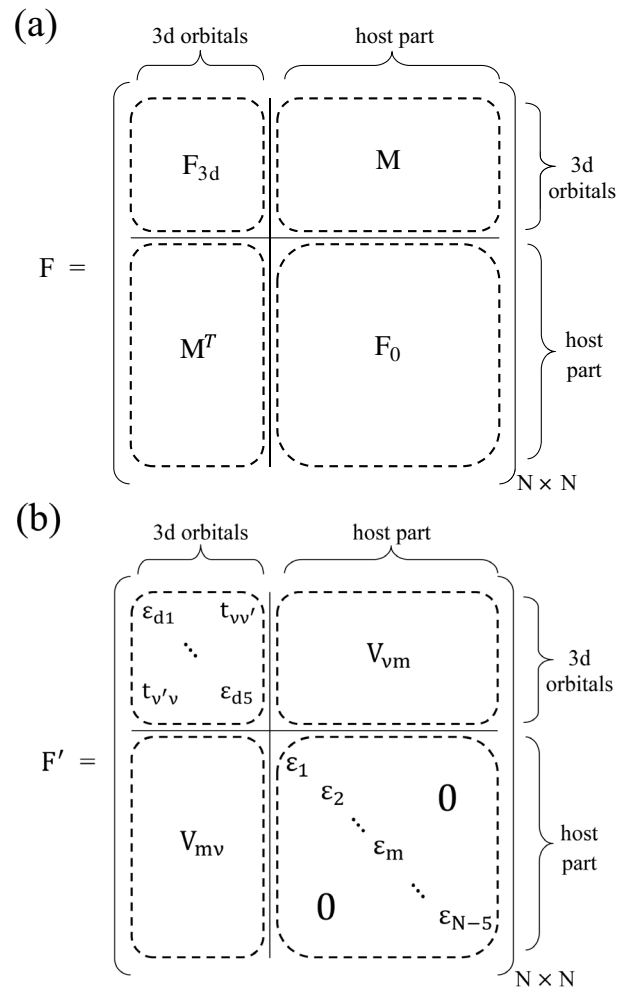Using the basis of the NAO's, the molecular orbitals $|\psi_n\rangle$ can be expressed as:

$$|\psi_n\rangle = \sum_{\nu=1}^{5} \beta_{n\nu}|\tilde{\phi}_{d\nu}\rangle + \sum_{i=1}^{N-5} \beta_{ni}|\tilde{\phi}_i\rangle, \tag{8}$$

where, $|\tilde{\phi}_{d\nu}\rangle$'s represent the five NAO's for the Co(3d_ν) orbitals, and $|\tilde{\phi}_i\rangle$'s represent the remaining NAO's. We have obtained the elements of the Fock matrix within the NAO basis by using the Gaussian program [31] along with the NBO 6.0 software package [33].

2.3 One-electron parameters of the Anderson Hamiltonian from the Fock matrix

Within the HF+QMC approach, we determine the one-electron parameters of the Anderson Hamiltonian from

Fig. 2. (a) Sketch of the Fock matrix $\mathbf{F}$ in the natural atomic orbital basis. Here, the 3d and the host parts of the Fock matrix are separated as $\mathbf{F}_{3d}$ and $\mathbf{F}_0$, respectively. The hybridization parts are $\mathbf{M}$ and $\mathbf{M}^T$. The host part $\mathbf{F}_0$ is not diagonal in the NAO basis. (b) Sketch of the Fock matrix $\mathbf{F}'$ which is obtained after diagonalizing the host part. We obtain the one-electron energies and the hybridization matrix elements of the effective Haldane-Anderson model from $\mathbf{F}'$. Eigenvalues of the host part of the Fock matrix $\mathbf{F}'$ yields ε_m, the host energy levels of the Anderson model. The off-diagonal matrix elements yield the hybridization parameters $V_{m\nu}$ between the host states and the Co(3d_ν) NAO's. Since $t_{\nu\nu'}$ are negligible, $\varepsilon_{d\nu}$'s become the energy levels of the impurity states.

the matrix elements of the Fock matrix expressed in the orthogonal NAO basis. This procedure is sketched in Figures 2a and 2b. Here, the $N \times N$ Fock matrix $\mathbf{F}$ consists of the 3d part $\mathbf{F}_{3d}$, the host part $\mathbf{F}_0$, and the hybridization parts $\mathbf{M}$ and its transpose $\mathbf{M}^T$ as illustrated in Figure 2a. The host part of the Fock matrix $\mathbf{F}_0$ is not diagonal in the NAO basis. By diagonalizing $\mathbf{F}_0$, we obtain the host energy levels ε_m of the effective Haldane-Anderson model, and the corresponding host eigenstates $|u_m\rangle$. In turn, the hybridization matrix elements $V_{m\nu}$ between the host eigenstates $|u_m\rangle$ and the Co(3d_ν) NAO's $|\tilde{\phi}_{d\nu}\rangle$ are obtained. We denote by $\mathbf{F}'$ the Fock matrix expressed in

---

[1] When we use the Gaussian 6-31G basis set in the Hartree-Fock calculation of the Fock matrix, the number of the basis functions including the Co(3d_ν) states is 347. This number increases to 504 when we use the Gaussian 6-31G(d) basis set. Since the QMC calculations require more computer time as the number of the host states increases, here we present results for the Gaussian 6-31G basis set. However, for comparison, we have also performed HF+QMC calculations by using the 6-31G(d) basis set for selected model parameters and we find negligible differences between the results for the 6-31G and 6-31G(d) basis sets.

the basis formed from the Co $(3d_\nu)$ NAO's and the orthogonal host states, which is illustrated in Figure 2b. We determine the one-electron parameters of the Anderson Hamiltonian from $\mathbf{F}'$. The impurity energies $\varepsilon_{d\nu}$ of the effective model are given by the diagonal matrix elements of $\mathbf{F}_{3d}$. We neglect the off-diagonal elements of $\mathbf{F}_{3d}$, which are denoted by $t_{\nu\nu'}$ in Figure 2b, since they are negligible in comparison to the diagonal terms.

Using the procedure outlined above, we obtain the model parameters ε_m, $\varepsilon_{d\nu}$, and $V_{m\nu}$ from the transformed Fock matrix $\mathbf{F}'$. Considering the effective Hamiltonian equation (1), we note that now $d^\dagger_{\nu\sigma}$ $(d_{\nu\sigma})$ creates (annihilates) a fermion in the Co $(3d_\nu)$ NAO state $|\tilde{\phi}_{d\nu}\rangle$, while $c^\dagger_{m\sigma}$ $(c_{m\sigma})$ creates (annihilates) a fermion in the orthogonal host eigenstate $|u_m\rangle$. Hence, the $V_{m\nu}$'s represent the hybridization matrix elements between the host eigenstates $|u_m\rangle$ and the Co $(3d_\nu)$ NAO's.

There have been many previous studies where the electronic structure calculations are combined with the many-body techniques [41]. The use of NAO's here for the case of a molecule is similar to the use of maximally-localized Wannier orbitals [42] to obtain the model parameters for various compounds [43,44].

2.4 Host density of states and the Co $(3d_\nu)$ energy levels

Figure 3a shows the total density of states $D(\varepsilon)$ defined by:

$$D(\varepsilon) = \sum_{n=1}^{N} \delta(\varepsilon - E_n) \qquad (9)$$

where E_n are the eigenvalues of the Fock matrix. Here, the highest occupied molecular orbital (HOMO) is located at -10.2 eV, and the lowest unoccupied molecular orbital (LUMO) is at -1.7 eV. Hence, the occupied and the unoccupied states are separated by an energy gap of 8.5 eV. In Figure 3b, the density of the host eigenstates defined by:

$$D_h(\varepsilon) = \sum_{m=1}^{N-5} \delta(\varepsilon - \varepsilon_m), \qquad (10)$$

where ε_m are the energy levels of the host eigenstates, is shown. We observe that in Figure 3b the HOMO and the LUMO levels are slightly shifted in comparison to Figure 3a. The energy levels of the Co $(3d_\nu)$ NAO states, $\varepsilon_{d\nu}$, are also shown as vertical lines in Figure 3b. We observe that the xz, x^2-y^2, and yz orbitals are degenerate and are much lower in energy with respect to the $3z^2 - r^2$ and xy orbitals, which are located above the energy gap and near the LUMO level.

In CNCbl, the 5 nitrogen atoms and the C atom surrounding Co form roughly a local octahedral environment for Co. Hence, the Co $(3d_\nu)$ levels separate into two groups, one containing the $3z^2-r^2$ and xy orbitals and the other containing the xz, x^2-y^2, and yz orbitals. This is similar to the separation of the $3d$ orbitals into the groups of e_g and t_{2g} orbitals in a crystal field with cubic symmetry. However, here we have taken a coordinate system
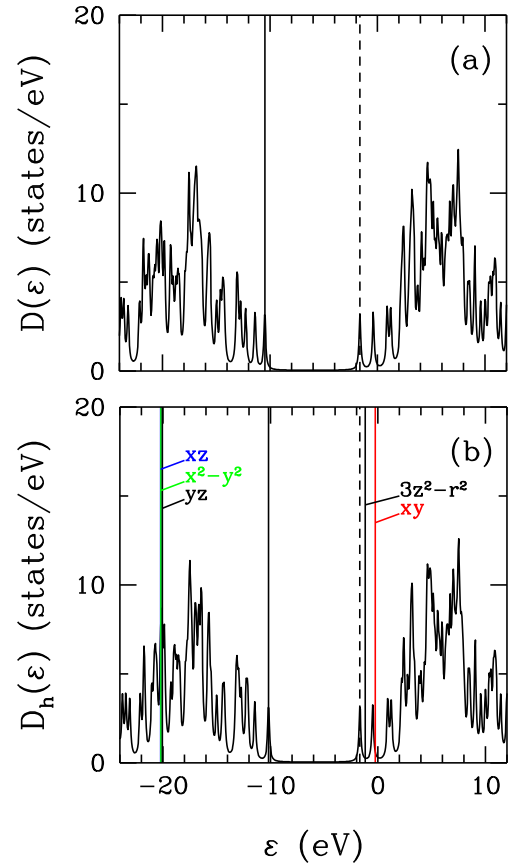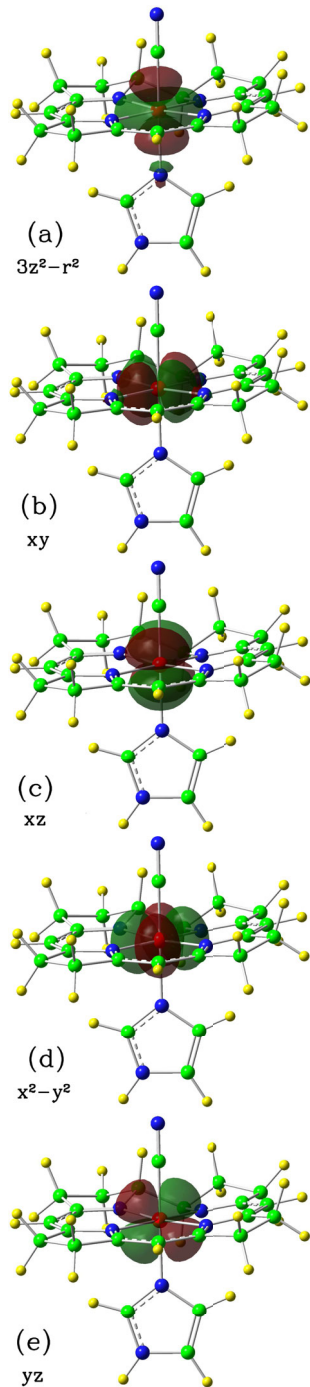

Fig. 3. (a) Total density of states of Im-[Co$^{\text{III}}$(corrin)]-CN$^+$, $D(\varepsilon)$, obtained within the Hartree-Fock approximation by using the Gaussian program. The vertical solid and dashed lines denote the HOMO and LUMO levels, respectively. (b) Density of states of the host eigenstates of the effective Haldane-Anderson model, $D_h(\varepsilon)$. Here, the HOMO and LUMO levels are slightly different than in (a). In addition, the energy levels of the Co $(3d_\nu)$ NAO's are indicated by the vertical lines.

such that the x and y axis are located at 45 degrees to the Co-N bond direction in the corrin layer instead of being parallel to the Co-N bond direction. Hence, the $x^2 - y^2$ and xy orbitals have been exchanged. In the following, because of our choice of the coordinate system which is the same as that of the Gaussian program, we will denote the $3z^2 - r^2$ and xy orbitals as the e_g-like states, and the xz, $x^2 - y^2$, and yz orbitals as the t_{2g}-like states.

At this point, it is useful to have a visual description of the Co $(3d_\nu)$ NAO states. In Figure 4, we show the Co $(3d_\nu)$ NAO's in terms of the atomic orbitals. Here, the e_g symmetry of the $3z^2 - r^2$ and xy NAO's is clearly seen as well as the t_{2g} symmetry of the xz, $x^2 - y^2$, and yz NAO's.
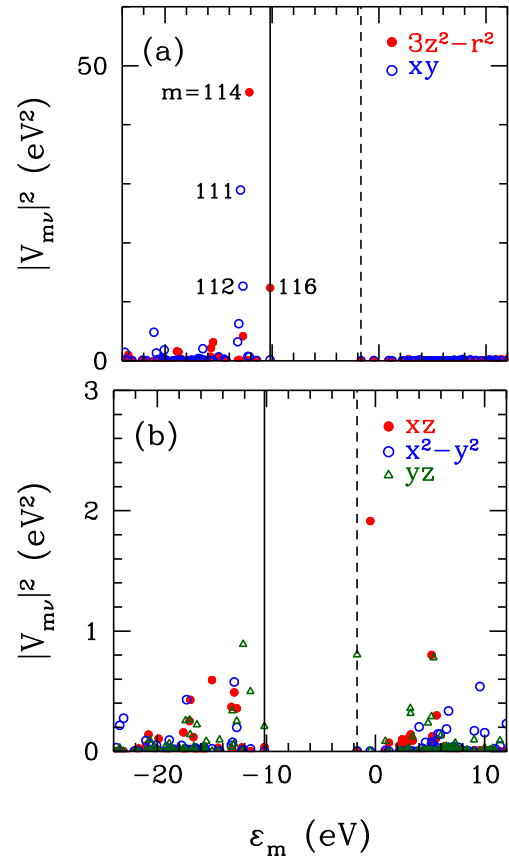
2.5 Host-Co $(3d_\nu)$ hybridization

In this section, we present Hartree-Fock data on the hybridization matrix elements of the Haldane-Anderson model, which were obtained as discussed in Subsection 2.3.

Fig. 5. Hartree-Fock results on the square of the hybridization matrix elements $|V_{m\nu}|^2$ between the host eigenstates $|u_m\rangle$ and the Co $(3d_\nu)$ NAO states $|\tilde{\phi}_{d\nu}\rangle$ plotted as a function of the energy of the mth host eigenstate ε_m. In (a) results are shown for the e_g-like $\nu = 3z^2 - r^2$ and xy orbitals, and in (b) for the t_{2g}-like $\nu = xz$, $x^2 - y^2$, and yz. Here, the vertical solid and dashed lines denote the HOMO and LUMO levels, respectively. We observe that the host states $m = 114, 111, 112$ and 116 have the strongest hybridization matrix elements. The matrix elements with the t_{2g}-like states are much smaller than those with the e_g-like states.

Fig. 4. Illustration of the Co $(3d_\nu)$ natural atomic orbitals in terms of the atomic orbitals. Color coding of the atomic sites is the same as in Figure 1b.

The square of the hybridization matrix elements $|V_{m\nu}|^2$ between the mth host eigenstate $|u_m\rangle$ and the Co $(3d_\nu)$ NAO are shown as a function of the host energy ε_m in Figures 5a and 5b. Here, we observe that the magnitude of $|V_{m\nu}|^2$ for the cobalt $3z^2 - r^2$ and xy orbitals can be an order of magnitude larger than those for xz, $x^2 - y^2$ and yz. This is not surprising since the $3z^2 - r^2$ and xy orbitals lie along the Co-N and Co-C bond directions according to

the coordinate system used here. Figure 5a shows that, for the $\nu = 3z^2 - r^2$ orbital, $|V_{m\nu}|^2$ has the largest values at $m = 114$ and 116. For $\nu = xy$, the largest values occur at $m = 111$ and 112. In Section 3, we will see that the host eigenstates $m = 114, 111, 112$ and 116 are the states which are most affected by the presence of the cobalt atom.

We note that $|V_{m\nu}|^2$'s have large values for a few host states, while being negligibly small for the remainder. This feature may be used in the future to increase the speed of the numerical calculations without losing accuracy.

2.6 Coulomb repulsion at the Co $(3d_\nu)$ orbitals

The intra-orbital Coulomb repulsion at the Co $(3d_\nu)$ atomic orbitals is given by the two-electron integral

$$U_\nu = \int d^3r \int d^3r' |\phi_{d\nu}(\mathbf{r})|^2 \frac{1}{|\mathbf{r} - \mathbf{r}'|} |\phi_{d\nu}(\mathbf{r}')|^2. \quad (11)$$

Using the 6-31G Gaussian basis set [31], we obtain $U_\nu = 36.8$ eV for the Co $(3d_\nu)$ orbitals. However, we note that the value of U_ν depends on which Gaussian basis set is used. While for the 3-21 basis set $U_\nu = 42.8$ eV, for the 6-31G and the 6-31G(d) sets, we obtain $U_\nu = 36.8$ eV.

Since the effective Anderson Hamiltonian introduced above uses the basis of the Co $(3d_\nu)$ NAO's, the Coulomb two-electron integrals also need to be evaluated in this basis instead of the basis of the Co $(3d_\nu)$ atomic orbitals. When we evaluate the inter-orbital Coulomb repulsion given by equation (11) using the Co $(3d_\nu)$ NAO's with the Gaussian 6-31G basis set, we obtain ≈ 28 eV.

In the remaining of this paper, we will use a constant U for U_ν, and present QMC results particularly for U varying between 28 eV and 36 eV. We are neglecting the inter-orbital Coulomb interactions in the QMC calculations, which are actually close in value to the intra-orbital terms. Hence, in the QMC part of the calculations, we are taking into account the effects of the Coulomb repulsion at a simple level, treating U more as a variable than a true ab initio parameter. Inclusion of the inter-orbital Coulomb interaction will clearly provide more accurate results as discussed in Subsection 4.4.

2.7 Double counting in HF+QMC

At this point, it is necessary to note that in the HF+QMC approach the onsite Coulomb repulsion U is taken into account twice, once in the Hartree-Fock calculation, and a second time in the QMC calculations. In order to prevent the double-counting of the effects of U in the many-body approaches which combine the electronic-structure calculations with the QMC simulations, a constant μ_{DC} is usually subtracted from the Co $(3d_\nu)$ levels [45–48], $\varepsilon_{d\nu} \rightarrow \tilde{\varepsilon}_{d\nu} = \varepsilon_{d\nu} - \mu_{DC}$. Here, μ_{DC} is given by

$$\mu_{DC} = U \frac{\langle n_d^{HF} \rangle}{10}, \qquad (12)$$

where $\langle n_d^{HF} \rangle$ is the total number of the electrons (including spin) in the Co $(3d)$ levels obtained within Hartree-Fock. Since the Hartree-Fock calculations yield $\langle n_d^{HF} \rangle = 6.8$, we use $\mu_{DC} = 0.68U$ in this paper.

It is possible to argue that, because we are using only the intra-orbital Coulomb repulsion in QMC, the double-counting shift should be orbital dependent and given by $\mu_{DC}^\nu = U \langle n_{d\nu}^{HF} \rangle / 2$, where $\langle n_{d\nu}^{HF} \rangle$ is the orbital dependent Co $(3d_\nu)$ occupation number including spin from the HF calculation. However, if we include the inter-orbital Coulomb interaction in QMC, then the shift would be orbital independent. Since we try to model the actual system as much as possible, we use a constant μ_{DC}.

In Figure 6, the shifted Co $(3d_\nu)$ NAO energy levels $\tilde{\varepsilon}_{d\nu}$ are shown for $U = 36$ eV and $\mu_{DC} = 0.68U$. Also, shown here is the host density of states $D_h(\varepsilon)$. For these parameters, the xz, x^2-y^2 and yz states are located below the bottom of the valence band, while the $3z^2-r^2$ and xy states are located in the middle.
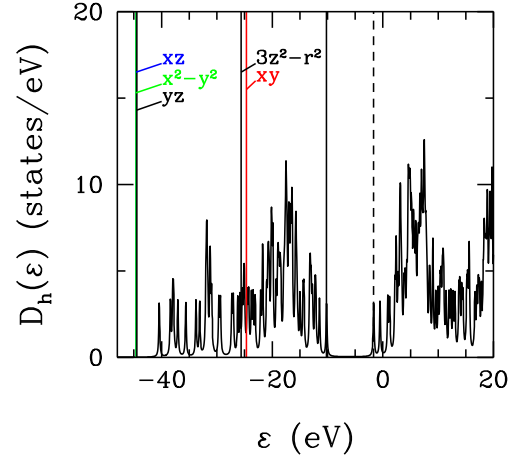
Fig. 6. Density of states of the host states of the effective Haldane-Anderson model $D_h(\varepsilon)$ from the Hartree-Fock calculation. Here, the Co $(3d_\nu)$ levels have been shifted by μ_{DC} in order to compensate for the double-counting of the Coulomb repulsion by the HF+QMC approach. The shift μ_{DC} has been evaluated for $U = 36$ eV.

3 Quantum Monte Carlo results

In this section, we present QMC data on the effective Haldane-Anderson model for Im-[Co^{III}(corrin)]-CN$^+$, of which parameters were obtained in the previous section. For this model, we have performed QMC calculations by using the Hirsch-Fye QMC algorithm [15]. In particular, we have calculated the Co $(3d_\nu)$ and the host single-particle Green's functions and the magnetic correlations functions.

In Section 3.1, we introduce the correlation functions which we evaluate with QMC. In Section 3.2, we present data on the electron occupation number and the magnetic moment formation at the Co $(3d_\nu)$ NAO's. Here, we observe that in-gap states develop arising from the Co $(3d_\nu)$ states in the semiconductor energy gap. The induced in-gap states reduce the value of the semiconductor gap found by the Hartree-Fock calculation. We find that the Co $(3d_\nu)$ states induced above the top of the valence band correspond to the upper Hubbard states of the Co t_{2g}-like orbitals. On the other hand, the Co $(3d_\nu)$ states induced in the middle of the semiconductor gap correspond to the impurity bound states originating from the Co e_g-like states. We reach this assignment based on the QMC results on the chemical potential dependence of the Co $(3d_\nu)$ electron occupation number and magnetic moment formation, host electron occupation numbers and magnetic moment formation as well as the antiferromagnetic correlations between the Co e_g states and the host eigenstates.

The QMC results on the host electrons are shown in Section 3.3. Here, we observe that the host electrons form new states inside the semiconductor gap at the same energies where the Co $(3d_\nu)$ NAO's develop in-gap states. These host states are the ones which have the strongest hybridization matrix elements with the Co e_g-like states. These host states also develop magnetic moments which

depend strongly on the electron filling of the impurity bound states.

In Section 3.4, we present data on the antiferromagnetic correlations which develop around the Co atom. We find that the antiferromagnetic correlations develop mainly between the Co e_g-like states and the electron spins at the CN axial ligand, and they depend strongly on the filling of the impurity bound states. The results presented in Section 3 are based on reference [49].

The QMC calculations are performed within the grand canonical ensemble, and the total electron number $\langle n_T \rangle$ is obtained by evaluating with QMC,

$$\langle n_T \rangle = \sum_{\nu=1}^{5} \sum_{\sigma} \langle d_{\nu\sigma}^\dagger d_{\nu\sigma} \rangle + \sum_{m=1}^{N-5} \sum_{\sigma} \langle c_{m\sigma}^\dagger c_{m\sigma} \rangle. \qquad (13)$$

In presenting the QMC data in the next section, we will obtain results as a function of μ and evaluate the corresponding $\langle n_T \rangle$ also with QMC. For the truncated structure Im-[Co^{III}(corrin)]-CN$^+$, the total electron number is $N_{el} = 238$. By comparing $\langle n_T \rangle$ with N_{el}, we obtain the corresponding value for μ.

3.1 QMC measurements

The Matsubara-time dependent single-particle Green's function for the Co $(3d_\nu)$ NAO states is defined by

$$G_{\nu\sigma}(\tau) = -\langle T_\tau d_{\nu\sigma}(\tau) d_{\nu\sigma}^\dagger(0) \rangle, \qquad (14)$$

where T_τ is the usual Matsubara τ-ordering operator and $d_{\nu\sigma}(\tau) = e^{H\tau} d_{\nu\sigma} e^{-H\tau}$. Similarly, the host Green's function is defined by

$$G_{m\sigma}(\tau) = -\langle T_\tau c_{m\sigma}(\tau) c_{m\sigma}^\dagger(0) \rangle. \qquad (15)$$

In addition, we calculate the square of the magnetic moment at each Co $(3d_\nu)$ orbital, $\langle (M_\nu^z)^2 \rangle$, where

$$M_\nu^z = d_{\nu\uparrow}^\dagger d_{\nu\uparrow} - d_{\nu\downarrow}^\dagger d_{\nu\downarrow}. \qquad (16)$$

In order to probe the magnetic correlations around the Co atom, we also calculate the equal-time Co $(3d_\nu)$-host magnetic correlation function $\langle M_\nu^z M_m^z \rangle$, where

$$M_m^z = c_{m\uparrow}^\dagger c_{m\uparrow} - c_{m\downarrow}^\dagger c_{m\downarrow}. \qquad (17)$$

We present data on $\langle (M_m^z)^2 \rangle$ as well. We note that this presentation of the QMC results on CNCbl is similar to the previous QMC study on the DMS materials [11,12].

In the following subsections, we show QMC data on the Co $(3d_\nu)$ electron number $\langle n_\nu \rangle$ and the square of the Co $(3d_\nu)$ moments $\langle (M_\nu^z)^2 \rangle$ as a function of the chemical potential μ. We also present data on the total host electron number $\langle n_h \rangle$ as well as the total electron number $\langle n_T \rangle$ as a function of μ. In addition, we study the local moment formation at the host eigenstates and their magnetic coupling to the Co $(3d_\nu)$ NAO's. We find that antiferromagnetic correlations develop between the Co e_g states and
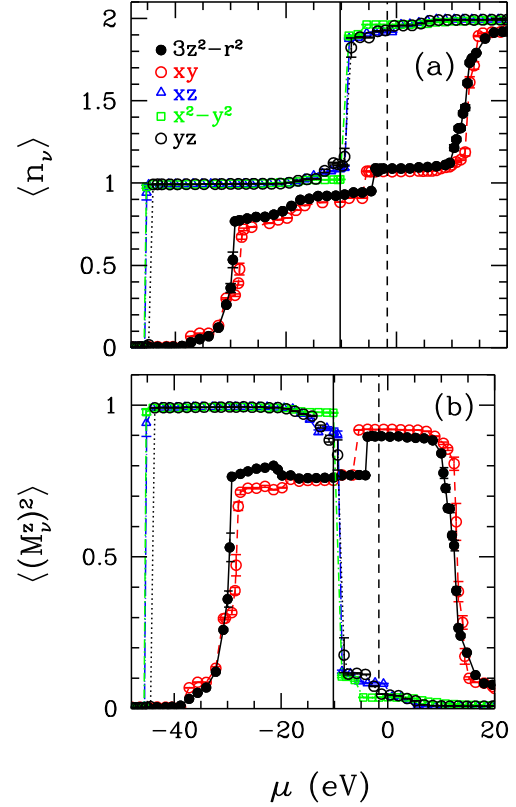
Fig. 7. (a) QMC results on the electron occupation number $\langle n_\nu \rangle$ of the Co $(3d_\nu)$ natural atomic orbitals plotted as a function of the chemical potential μ. (b) Square of the magnetic moment $\langle (M_\nu^z)^2 \rangle$ at the Co $(3d_\nu)$ natural atomic orbitals versus the chemical potential μ. Here, the vertical solid and dashed lines denote the HOMO and the LUMO levels, respectively. These results are for $U = 36$ eV.

the electronic spins at the CN axial ligand depending on the value of μ.

In obtaining the QMC data shown below, Matsubara-time discrete steps between $\Delta\tau = 0.04$ eV^{-1} and 0.07 eV^{-1} were used. The results are presented for temperature $T = 2000$ K in the grand canonical ensemble. Hence, a temperature broadening of order 0.17 eV is expected for the energy resolution of the QMC data.

3.2 QMC results on the Co $(3d_\nu)$ electrons

We begin presenting QMC data with Figure 7a which shows the electron number $\langle n_\nu \rangle$ of the Co $(3d_\nu)$ NAO states as a function of the chemical potential μ for $U = 36$ eV. Similarly, Figure 7b shows the square of the magnetic moment $\langle (M_\nu^z)^2 \rangle$ at the Co $(3d_\nu)$ orbitals as a function of μ. We observe that the results for the Co $(3d)$ xz, $x^2 - y^2$, and yz states are similar to each other. The results for the $3z^2 - r^2$ and xy states are also similar. From the μ dependence shown in these figures it is possible to extract information on the single-particle spectral weight distribution and the local moment formation.

The bare energy levels $\tilde{\varepsilon}_{d\nu}$ of the Co $(3d)$ xz, $x^2 - y^2$, and yz NAO states are almost degenerate and are located

at $\varepsilon \approx -45$ eV below the lower edge of the valence band, as seen in Figure 6. In Figure 7a we see that for these orbitals $\langle n_\nu \rangle$ exhibits a jump of unit magnitude at $\mu \approx -45$ eV. These orbitals remain singly occupied as μ is increased upto the interval -10 eV $\lesssim \mu \lesssim -8$ eV, at which point these orbitals become nearly doubly occupied. In Figure 7b, we see that the magnetic moments at these orbitals have their maximum value in the interval -45 eV $\lesssim \mu \lesssim -10$ eV. Above ≈ -10 eV, these moments decrease rapidly due to double occupancy. The in-gap states in the energy interval -10 eV $\lesssim \varepsilon \lesssim -8$ eV have sufficient spectral weight to accommodate a total of nearly three electrons, and their location corresponds to approximately $\tilde{\varepsilon}_{d\nu} + U$. Hence, we deduce that these in-gap states correspond to the upper-Hubbard states of the Co t_{2g}-like orbitals. We note that they are located inside the gap, and hence new impurity states are formed inside the gap found by HF.

Figure 6 shows that the bare energy levels $\tilde{\varepsilon}_{d\nu}$ of the $3z^2 - r^2$ and xy orbitals are near -25 eV. In Figure 7a we observe that for these two orbitals, $\langle n_\nu \rangle$ becomes finite at $\mu \approx -38$ eV, increases rapidly around $\mu \approx -30$ eV, and remains less than one until μ reaches ≈ -5.5 eV. This type of μ dependence suggests that the $U = 0$ single-particle spectral weight, which is a δ-function near -25 eV, has been shifted down in energy and has been broadened. These orbitals remain less than singly occupied until μ reaches ≈ -5.5 eV, where $\langle n_{xy} \rangle$ exhibits a sudden increase of about 0.2. We think that this sudden increase corresponds to an impurity bound state as found in the mean-field solution of the Haldane-Anderson model [13]. For the $3z^2 - r^2$ orbital, a similar increase occurs at a slightly higher energy of ≈ -4 eV. We note that these jumps take place in the energy gap found by HF. Hence, new impurity states are formed in the energy gap. As seen in Figure 7b, the magnetic moments at the xy and $3z^2 - r^2$ orbitals also exhibit sudden increases at these energies. The occupation numbers of these states remain constant at unit magnitude as μ is increased upto ≈ 10 eV. This value of μ corresponds approximately to $\tilde{\varepsilon}_{d\nu} + U$ for the xy and $3z^2 - r^2$ orbitals. Above this energy, the xy and $3z^2 - r^2$ orbitals rapidly become doubly occupied, and the magnetic moments decrease.

In summary, from Figure 7a we deduce that new in-gap states originating from the Co (3d) xz, $x^2 - y^2$ and yz orbitals form in the energy interval -10 eV $\lesssim \varepsilon \lesssim -8$ eV, while new states from the xy and $3z^2 - r^2$ orbitals form at energies ≈ -5.5 eV and ≈ -4 eV, respectively. These newly formed states reduce the value of the semiconductor gap found by the Hartree-Fock calculation, which is 8.5 eV, down to ≈ 3 eV.

Figure 8a shows the QMC data on the total electron occupation of the Co $(3d_\nu)$ states

$$\langle n_d \rangle = \sum_{\nu=1}^{5} \sum_{\sigma} \langle d_{\nu\sigma}^\dagger d_{\nu\sigma} \rangle \qquad (18)$$

versus the chemical potential μ. Here, results are shown for various values of U in order to see the dependence
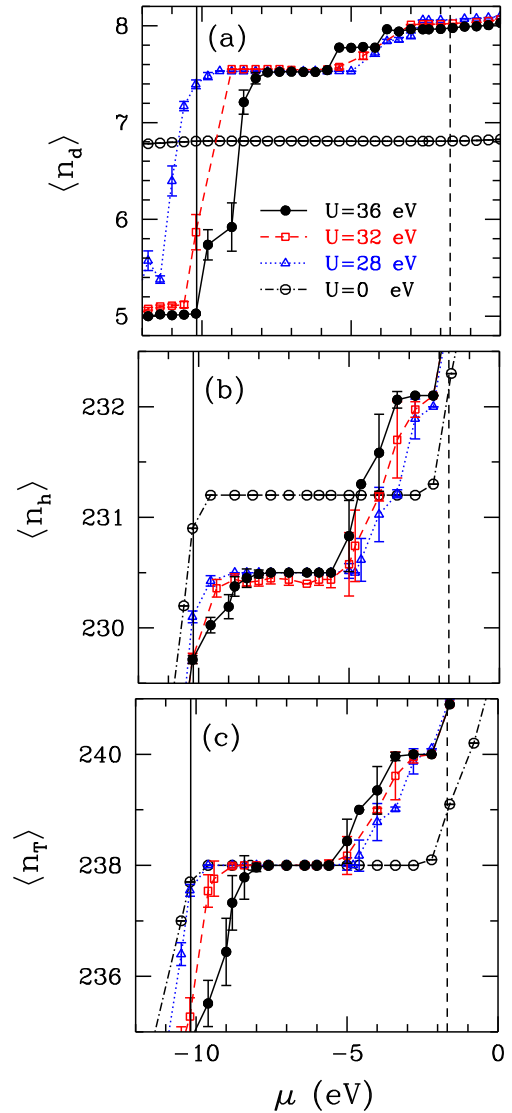
Fig. 8. (a) Total electron occupation number $\langle n_d \rangle$ of the Co (3d) natural atomic orbitals as a function of the chemical potential μ. (b) Total number of the host electrons $\langle n_h \rangle$ versus μ. (c) Total number of electrons, $\langle n_T \rangle = \langle n_d \rangle + \langle n_h \rangle$, versus μ. Here, results are shown for various values of the intra-orbital Coulomb repulsion U. In addition, the vertical solid and dashed lines denote the Hartree-Fock results for the HOMO and LUMO levels, respectively.

on U. We note that in these calculations, as U is varied, $\tilde{\varepsilon}_{d\nu}$ also varies according to equation (12).

For $U = 36$ eV, we observe that $\langle n_d \rangle$ increases as μ is varied from -10 eV to -8 eV, because the xz, $x^2 - y^2$ and yz orbitals become nearly doubly occupied in this interval. In the energy gap, for -8 eV $\lesssim \mu \lesssim -5.5$ eV, we get $\langle n_d \rangle \approx 7.55$. In comparison, the X-ray scattering experiments find that the value of $\langle n_d \rangle$ in CNCbl is 7.7 ± 0.1 [22]. Above $\mu \approx -5.5$ eV, we observe two step-like increases in $\langle n_d \rangle$ coming from the xy and $3z^2 - r^2$ states. For $U = 36$ eV, the energy gap between the highest occupied and the lowest unoccupied Co (3d) levels is ≈ 3 eV. In comparison, the experimental value for the

semiconductor gap of CNCbl is about 2.2 eV [6]. As U is decreased from 36 eV to 28 eV, we observe that the in-gap states move closer to the semiconductor gap edges, and the magnitude of the energy gap increases.

Also shown in Figure 8a are results for $U = 0$, in which case we obtain $\langle n_d \rangle = 6.8$ in the interval -12 eV $\leq \mu \leq 0$ eV. As seen in Figure 3b, for $U = 0$, the bare energy level for the xz, $x^2 - y^2$ and yz orbitals is ≈ -20 eV, while for the $3z^2 - r^2$ and xy orbitals one has ≈ -1 eV and ≈ 0 eV, respectively. If the hybridization is turned on while keeping $U = 0$, then spectral weight of the $3z^2 - r^2$ and xy orbitals are broadened and shifted to higher energies. For this reason, $\langle n_d \rangle$ remains constant in the interval -12 eV $\leq \mu \leq 0$ eV for $U = 0$.

Finally, we note that the hybridization matrix elements $V_{m\nu}$'s are dependent on the atomic coordinates used in the HF calculation. Because of uncertainties in the atomic coordinates, it is necessary to study how the general features of the single-particle spectrum depend on $V_{m\nu}$. With this in mind, we have repeated the above QMC calculations by reducing the hybridization matrix elements by 10%. In this case, we found that, for $U = 36$ eV, the lowest energy impurity bound state occurs at ≈ -6.5 eV instead of -5.5 eV, and the energy gap is reduced to ≈ 2 eV. Hence, we see that the impurity bound state is robust with respect to small variations in $V_{m\nu}$. This is important because the values of the $V_{m\nu}$'s depend on the Co-C bond length, and we are using simple estimates for the geometrical parameters as described in the introduction of Section 2.
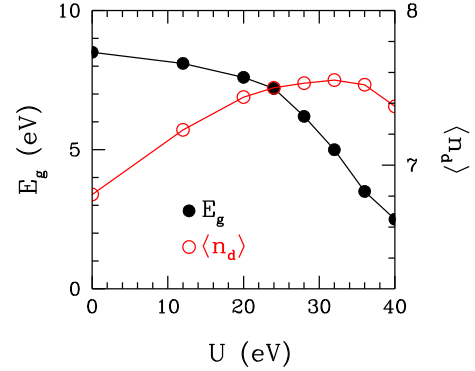
3.3 QMC results on the host electrons

Figure 8b shows the total number of the host electrons

$$\langle n_h \rangle = \sum_{m=1}^{N-5} \sum_{\sigma} \langle c_{m\sigma}^{\dagger} c_{m\sigma} \rangle, \tag{19}$$

where $N = 347$, plotted as a function of the chemical potential μ. Comparing Figures 8a and 8b, we observe that $\langle n_h \rangle$ and $\langle n_d \rangle$ exhibit jumps at the same values of μ. Hence, the host states also develop spectral weight inside the gap at the same energies as the Co $(3d_\nu)$ states. We note that the error bars in the data on $\langle n_h \rangle$ are larger than in $\langle n_d \rangle$, since the QMC calculation of $\langle n_h \rangle$ is computationally more costly.

For the interval -10 eV $\lesssim \varepsilon \lesssim -8$ eV, the jump in $\langle n_d \rangle$ is ≈ 2.5, while the jump in $\langle n_h \rangle$ is ≈ 0.5. On the other hand, we note that, in the interval -5.5 eV $\lesssim \varepsilon \lesssim -2$ eV, the jump in $\langle n_h \rangle$ is about ≈ 1.6, while that in $\langle n_d \rangle$ is ≈ 0.4. Hence, actually there are more host states induced in the gap for ≈ -5.5 eV $\lesssim \varepsilon \lesssim -2$ eV than from the Co $(3d_\nu)$ orbitals.

The total number of the electrons $\langle n_T \rangle = \langle n_d \rangle + \langle n_h \rangle$ versus μ is shown in Figure 8c. For Im-[Co$^{\text{III}}$(corrin)]-CN$^+$, the total electron number is 238. From this figure we identify $\mu \approx -8.5$ eV as the new value of the HOMO level, and $\mu \approx -5.5$ eV as the new LUMO level. Here, we also observe that the in-gap states located in the interval -5.5 eV $\lesssim \mu \lesssim -3.5$ eV have sufficient spectral weight

Fig. 9. HF+QMC results on the energy gap E_g between the HOMO and LUMO states versus the intra-orbital Coulomb repulsion U (left axis). Total electron number at the Co $(3d)$ orbitals, $\langle n_d \rangle$ when the chemical potential is in the energy gap, versus U (right axis). Here, μ_{DC} which shifts the bare Co $(3d_\nu)$ energy levels is varied along with U according to equation (12).

to accommodate a total of two electrons. In comparison, the in-gap states in -10 eV $\lesssim \mu \lesssim -8$ eV accommodate 3 electrons.

We also note that $\tilde{\varepsilon}_{d\nu}$ for $3z^2 - r^2$ and xy states are near -25 eV. Hence, for $U = 36$ eV, the doubly-occupied states occur at $\mu \approx \tilde{\varepsilon}_{d\nu} + U = 11$ eV. Hence, the in-gap states which form from the $3z^2 - r^2$ and xy orbitals do not originate from the upper Hubbard states. Instead, they are similar in origin to the impurity bound states found in the mean-field solution of the Haldane-Anderson model of a transition-metal impurity in a semiconductor host [13].

Since for Im-[Co$^{\text{III}}$(corrin)]-CN$^+$ the total electron number is 238, in Figure 8c we see that the effective energy gap decreases as U is increased. For $U = 36$ eV, the effective energy gap becomes ≈ 3 eV. Hence, the energy gap can be significantly reduced with respect to the Hartree-Fock value of 8.5 eV.

The values of the effective energy gap are plotted in Figure 9 as a function of U. We note that in this calculation, as U is varied, the shift μ_{DC} is also varied according to equation (12). Also plotted in Figure 9 is $\langle n_d \rangle$ versus U. For $\langle n_d \rangle$, the experimental estimate [22] is 7.7±0.1. Hence, for $U \approx 36$ eV, HF+QMC yields values for the energy gap and $\langle n_d \rangle$ which are comparable to the experimental values. For this reason, in the remainder of this paper we will present QMC data for $U = 36$ eV.

We next explore the nature of the in-gap states originating from the host eigenstates. In particular, we are interested in understanding which atomic orbitals contribute to these host states induced in the energy interval between ≈ -5.5 eV and ≈ -2.0 eV. In order to achieve this, we study how the electron occupation of the host states $\langle n_m \rangle$ changes as μ is varied from below this energy interval to above it. In particular, we show how $\langle n_m \rangle$ changes as μ is varied from -7.0 eV to -2.2 eV. For this purpose, we first show in Figure 10a the electron occupation of the host eigenstates $\langle n_m \rangle$ as a function of the host energy ε_m at $\mu = -7.0$ eV for $U = 36$ eV. We note that for $\mu = -7.0$ eV, the host states located between ≈ -5.5 eV
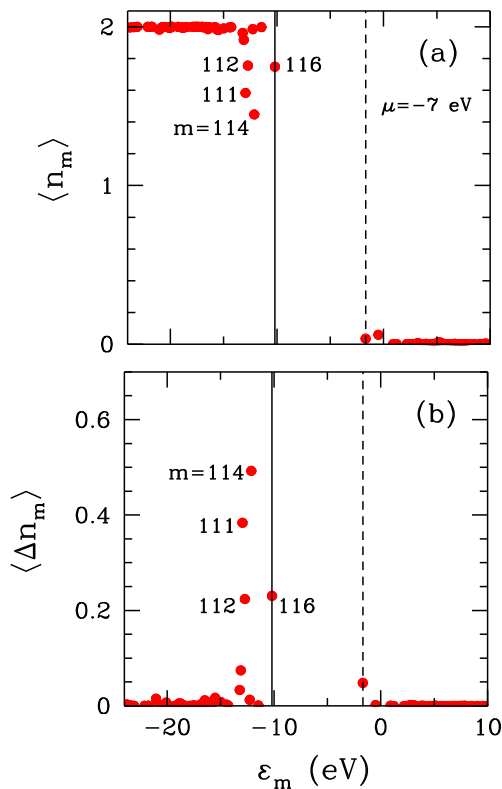
Fig. 10. (a) Occupation number of the host eigenstates $\langle n_m \rangle$ versus the host energy ε_m for chemical potential $\mu = -7.0$ eV. Here, we see that the host eigenstates $m = 111, 112, 114$ and 116 are not doubly occupied even though the corresponding ε_m are located deep below μ. (b) Difference in the occupation number of the mth host eigenstate as μ is changed from -7.0 eV to -2.2 eV, $\langle \Delta n_m \rangle = \langle n_m \rangle|_{\mu=-2.2 \text{ eV}} - \langle n_m \rangle|_{\mu=-7.0 \text{ eV}}$, plotted as a function of ε_m. These results are for $U = 36$ eV. In addition, here, the vertical solid and dashed lines denote the HOMO and the LUMO levels, respectively.

and ≈ -2.0 eV are not occupied by electrons yet. Even though here we use $\mu = -7.0$ eV, any value of μ in the energy gap between ≈ -8.0 eV and ≈ -5.5 eV gives similar results. In Figure 10a, we observe that, for this value of μ, there are valence-band host eigenstates which are not doubly occupied even though they are located deep below the chemical potential. In particular, the host eigenstates with labels $m = 114, 111, 112$ and 116 exhibit the most reduced values of $\langle n_m \rangle$. We note that these host eigenstates have the strongest hybridization matrix elements with the $3z^2 - r^2$ and xy orbitals, as it was seen in Figure 5a.

Next, we change μ from -7.0 eV to -2.2 eV, and plot the increase in $\langle n_m \rangle$, $\langle \Delta n_m \rangle = \langle n_m \rangle|_{\mu=-2.2 \text{ eV}} - \langle n_m \rangle|_{\mu=-7.0 \text{ eV}}$, as a function of the host energy ε_m in Figure 10b. We already know from Figure 8b that, for $U = 36$ eV, the in-gap states become fully occupied when $\mu \approx -2.0$ eV. Hence, the change $\langle \Delta n_m \rangle$ as μ goes from -7.0 eV to -2.2 eV represents how much the occupation of the host states changes as the impurity bound states located in the interval between ≈ -5.5 eV and ≈ -2.0 eV become occupied. In other words, $\langle \Delta n_m \rangle$ represents how much individual host eigenstates contribute to the impu-
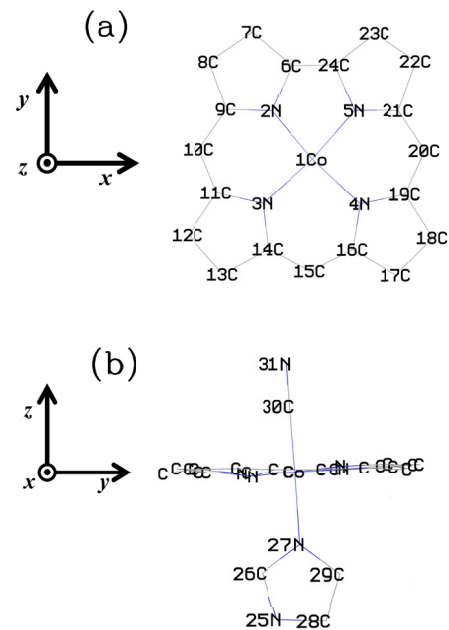

Fig. 11. (a) Top view of Im-[Co$^{\text{III}}$(corrin)]-CN$^+$. We note that the x and y axes are located at 45 degrees to the Co-N bonds in the corrin plane, and the z axis is perpendicular to the corrin plane. (b) Side view of Im-[Co$^{\text{III}}$(corrin)]-CN$^+$, where the imidazole and CN ligands attached to Co below and above the corrin ring, respectively, are seen. Here, the carbon and nitrogen atoms have been labelled for convenience, while the hydrogen atoms are not shown.

rity bound state. Here, we see that the largest increase in $\langle n_m \rangle$ takes place for $m = 114, 111, 116$ and 112. The rest of the host eigenstates exhibit negligible change as μ is increased from -7.0 eV to -2.2 eV. Hence, the impurity bound states derive mainly from the $m = 114, 111, 116$ and 112 host eigenstates. In turn, within the rigid-band picture, it is possible to state that the host eigenstates $m = 114, 111, 116$ and 112 have significant amount of single-particle spectral weight between energies -7.0 eV and -2.2 eV, which have been generated by the Coulomb repulsion and the hybridization.

In order to gain insight into the real-space structure of the in-gap host eigenstates located in the interval between ≈ -5.5 eV and ≈ -2.0 eV, we study the NAO composition of these host eigenstates. However, before doing so, it is useful to discuss briefly the geometrical structure of Im-[Co$^{\text{III}}$(corrin)]-CN$^+$, which is sketched in Figure 11. Figure 11a shows a top view of the corrin ring around the Co atom in Im-[Co$^{\text{III}}$(corrin)]-CN$^+$. Here, we have only shown the C and N atoms around Co, and have not included the H atoms. According to our coordinate system, which is the same as that of the Gaussian program, the corrin ring lies in the xy plane, and the x and y axes make 45 degrees with the Co-N bond directions. Figure 11b shows the side view of Im-[Co$^{\text{III}}$(corrin)]-CN$^+$. Here, we see the imidazole ring attached to Co below the corrin plane and the CN axial ligand attached to Co above the corrin plane. Here, the C
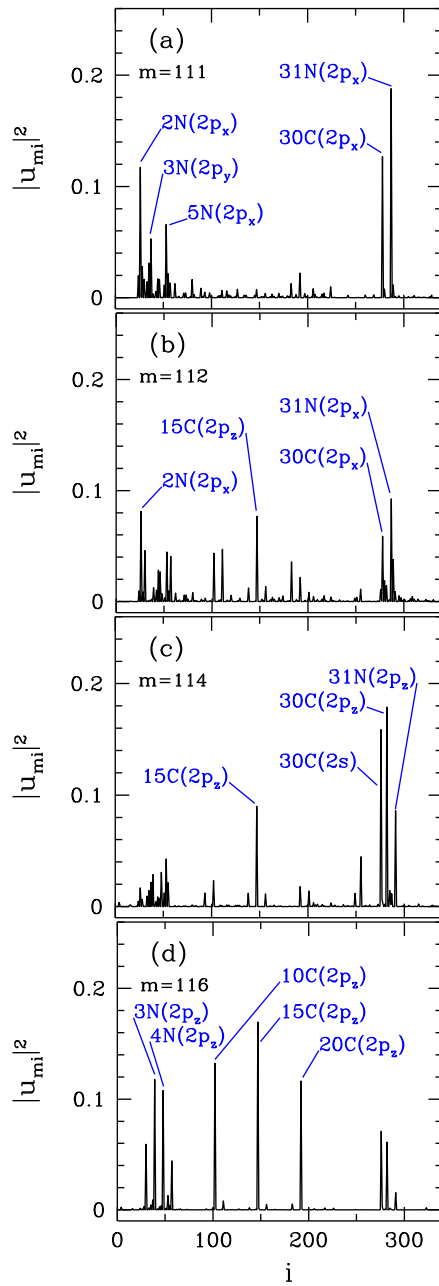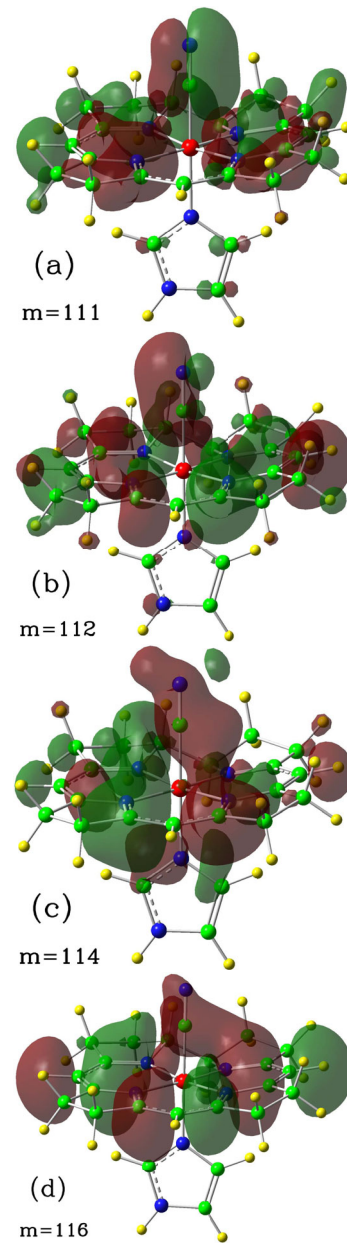
Fig. 12. NAO weight of the mth host eigenstate $|u_{mi}|^2 = |\langle \tilde{\phi}_i | u_m \rangle|^2$ versus the label i of the host NAO for (a) $m = 111$, (b) 112, (c) 114, and (d) 116. The maximum value for index i is 342, which is the total number of the host NAO's.

Fig. 13. Real-space structure around the Co site of the $m = 111$, 112, 114, and 116th host states in terms of the atomic orbitals. Color coding of the atomic sites is the same as in Figure 1b.

and N atoms in the axial ligand are labelled as 30C and 31N as in the notation of the Gaussian program.

Figure 12a shows the NAO composition of the $m = 111$th host eigenstate. In particular, here we plot the NAO weight of the $m = 111$th host eigenstate defined as

$$|u_{mi}|^2 = |\langle \tilde{\phi}_i | u_m \rangle|^2 \tag{20}$$

versus the label i of the host NAO state. In this figure, we have labeled only the NAO states which have the dominant contribution; the NAO states with smaller weights

are not labeled here. Figures 12b–12d show similar results for the $m = 112$, 114 and 116th host states. In these figures, we see that the $m = 111$ and 112th states have large weight from the $2p\pi$ NAO's of the CN axial ligand. Similarly, the $m = 114$ host state mainly consists of the $2p\sigma$ NAO's of the CN axial ligand. On the other hand, the $m = 116$ host state consists of the $2p\sigma$ NAO's on the 10th, 15th and 20th C sites as well as N sites located around Co in the corrin plane as sketched in Figure 11a.

In order to have further physical insight into these host states, it is useful to have a visual description. For this purpose, we have obtained the composition of these host states in terms of the atomic orbitals. Figure 13 shows an
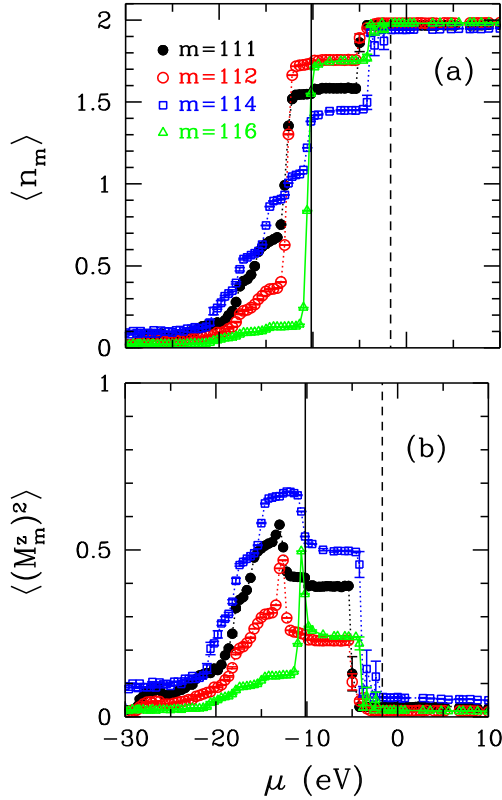
Fig. 14. (a) Occupation of the mth host eigenstate $\langle n_m \rangle$ versus μ. (b) Square of the magnetic moment of the mth host eigenstate $\langle (M_m^z)^2 \rangle$ versus μ. Here, the vertical solid and dashed lines denote the HOMO and the LUMO levels, respectively. In addition, these results are for $U = 36$ eV.

illustration of the $m = 111$, 112, 114 and 116th host states in terms of the atomic orbitals. We note that since the impurity bound states mainly include contributions from these host states, the impurity bound states also exhibit this type of real-space structure around the Co site.

In Figure 14, we show results on the occupation number and the magnetic moment for the same host eigenstates $m = 111$, 112, 114 and 116. Figure 14a shows the occupation number $\langle n_m \rangle$ versus μ for these host eigenstates. We observe that a sharp increase in $\langle n_m \rangle$ occurs at $\mu \approx \tilde{\varepsilon}_m$ in the valance band. We see that the single-particle spectral weight of the $m = 111$th host state is broadened in the valence band. In addition, a step-like increase exists inside the energy gap at ≈ -5.5 eV, above which this host state reaches double occupancy. Similar μ dependencies are observed for the others. The host state $m = 112$ also exhibits a jump at ≈ -5.5 eV, while for $m = 114$ and 116 the jump occurs at ≈ -4 eV. The jumps in $\langle n_m \rangle$ are largest for $m = 114$ and 111.

Figure 14b shows the square of the magnetic moment $\langle (M_m^z)^2 \rangle$ for the same host eigenstates. We observe that significant size moments develop for these host states until the in-gap states become occupied. As the in-gap host states are filled and they approach double-occupancy, the magnetic moments decrease rapidly.

Finally, we note that the states induced in the interval -10 eV $\lesssim \varepsilon \lesssim -8$ eV originate mainly from the Co t_{2g}-like states. In Figures 8a–8c, we observe that in this interval there is sufficient spectral weight to accommodate 3 electrons, of which about 2.5 electrons have the Co t_{2g}-like character. The remaining 0.5 electrons originate from the $m = 115$ host state, which mainly consists of the $2p\pi$ orbitals of the C and N atoms in the corrin ring. We do not show the composition of the $m = 115$th host state in order not to increase the length of the manuscript.
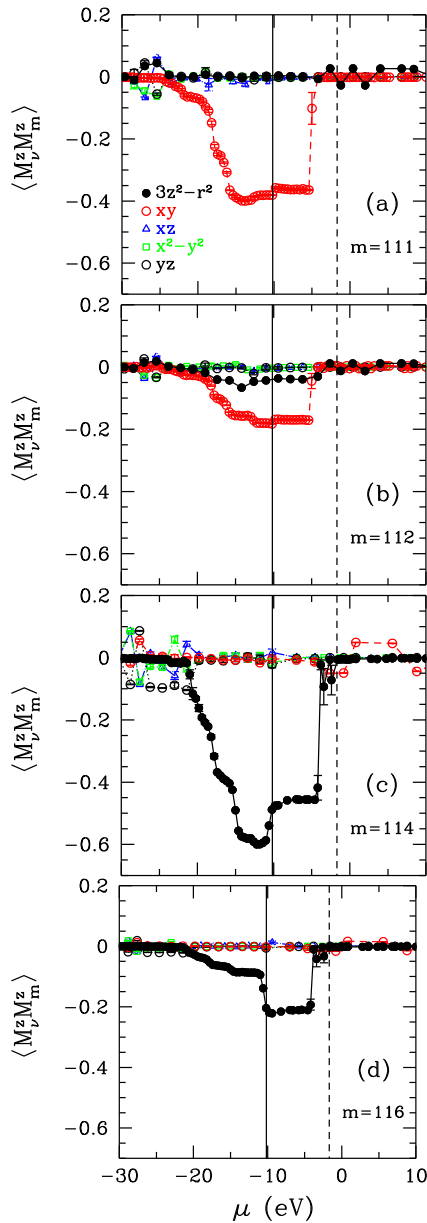
3.4 QMC results on the Co $(3d_\nu)$-host magnetic correlations

In Figure 15, we discuss the magnetic correlations between the Co $(3d_\nu)$ electrons and the host eigenstates $m = 111$, 112, 114 and 116. In particular, these figures show the magnetic correlation function $\langle M_\nu^z M_m^z \rangle$ between the Co $(3d_\nu)$ state and the mth host eigenstate plotted as a function of μ.

In Figures 15a and 15b we observe that the Co $(3d_{xy})$ NAO develops antiferromagnetic correlations with the $m = 111$ and 112th host states. These antiferromagnetic correlations diminish rapidly as the in-gap state located at ≈ -5.5 eV becomes occupied. The $m = 111$ and 112th states do not exhibit magnetic correlations with the other Co $(3d_\nu)$ orbitals. In Figures 15c and 15d we observe that the Co $(3d_{3z^2-r^2})$ NAO develops antiferromagnetic correlations with the $m = 114$ and 116th host states. In Figures 12a–12c, we have seen that the $m = 111$, 112 and 114th states contain large weight of the NAO's localized at the CN axial ligand. Thus we deduce that the electrons at the CN axial ligand develop antiferromagnetic correlations with the Co e_g orbitals. These antiferromagnetic correlations diminish rapidly when the impurity bound states become filled with electrons. Hence, as Im-[Co^{III}(corrin)]-CN$^+$ goes from the $N_{el} = 238$ state to $N_{el} = 239$ and 240 states, the antiferromagnetic correlations between the CN ligand and the Co e_g electrons disappear rapidly. We note that the $m = 116$ host state contains spectral weight from the $2p\sigma$ NAO's at the C and N sites in the corrin ring as seen in Figure 12d. Figure 15d shows that these NAO's also develop antiferromagnetic correlations with the Co $(3d_{3z^2-r^2})$ orbital.

It is important to note that we identify the in-gap induced states at ≈ -5.5 eV and ≈ -4 eV as impurity bound states because of the μ dependencies discussed in Figures 7, 8, 14 and 15. Similar behaviour is obtained in studying the impurity bound states found in the DMS materials [10–12].

We have also studied the magnetic correlations between the magnetic moments forming at the Co $3d_{3z^2-r^2}$ and $3d_{xy}$ orbitals. We find that these orbitals exhibit only weak magnetic correlations. This is different than the case for the DMS materials, where an indirect ferromagnetic coupling is generated between two impurity moments due to their antiferromagnetic coupling to the same continuum of host electrons [10–12]. Here, the Co $3d_{3z^2-r^2}$ and $3d_{xy}$ orbitals do not have strong hybridization with the

Fig. 15. Magnetic correlation function $\langle M_\nu^z M_m^z \rangle$ between the mth host eigenstate and the various the Co $(3d_\nu)$ NAO's. Here, results are shown for host eigenstates (a) $m = 111$, (b) 112, (c) 114, and (d) 116. In addition, the vertical solid and dashed lines denote the HOMO and the LUMO levels, respectively. These results are for $U = 36$ eV.

same host eigenstates as seen in Subsection 2.5. In modelling the DMS materials, a continuum of host states with constant hybridization is used, while for CNCbl the host eigenstates have discrete energy levels with varying hybridization matrix elements. Hence, an indirect ferromagnetic coupling is not generated. However, the inclusion of the Hund's coupling can generate a ferromagnetic coupling between the magnetic moments at the Co $3d_{3z^2-r^2}$ and $3d_{xy}$ NAO's.

It would be interesting to probe experimentally the antiferromagnetic correlations found in the HF+QMC

calculations. It is known that Cbl exhibits weak diamagnetism [50,51], which has been intepreted as Co in Cbl having a low spin state. This is also partly responsible for the notion that the interaction effects are not important in Cbl. In the HF+QMC results, we see that magnetic moments can develop in the Co e_g orbitals and in the host eigenstates coupled to these orbitals. It is possible to calculate the magnetic susceptibility within HF+QMC in order to extract the effective moment size for Co and the whole molecule. But such a calculation would be more meaningful after including the Hund's coupling.

4 Discussion

In this section, we discuss the meaning and implications of the HF+QMC data shown in Section 3. For this purpose, in Subsection 4.1, we compare the HF+QMC data with the DFT calculations on the same truncated molecule Im-[Co^{III}(corrin)]-CN$^+$. We find that there are important differences between the results of these two approaches. In particular, while the HF+QMC calculations for the Haldane-Anderson model find that the LUMO state corresponds to an impurity bound state, this is not the case for the DFT results. In Subsection 4.2, we compare the HF+QMC data with the photoabsorption experiments on CNCbl. Here, we discuss the nature of the lowest excited states in the photoabsorption spectrum. The HF+QMC data suggest that the lowest-energy excitations are dominated by electron transfer from the Co t_{2g}-like orbitals to the impurity bound states which contain spectral weight mainly from the CN axial ligand and the corrin ring. In Subsection 4.3, we note that the DFT+QMC method may also be applied to the same problem. In Subsection 4.4, we emphasize the importance of including the inter-orbital Coulomb repulsion and the Hund's coupling.

4.1 Comparison of the HF+QMC data with the DFT results

Various DFT based calculations have been performed for Cbl [16–26]. In this subsection, we compare the HF+QMC data obtained for Im-[Co^{III}(corrin)]-CN$^+$ by using the Haldane-Anderson model with the results obtained from the density functional theory (DFT) calculations on the same truncated molecule. We note that these DFT results are similar to the results of the time-dependent DFT calculations on the same system [24].

Figure 16 shows the total density of states $D(\varepsilon)$ versus ε for Im-[Co^{III}(corrin)]-CN$^+$ obtained by using the Gaussian program [31] with the 6-31G basis set and the BP86 exchange correlation potentials [37,38]. Here, the solid and dashed vertical red lines denote the HOMO and LUMO levels obtained by DFT. According to the DFT results the energy gap is ≈2.2 eV, which is in agreement with the experimental results. The vertical black lines, on the other hand, denote the HOMO and LUMO levels obtained by the HF calculations shown in Figure 3a. Comparing the HF results on $D(\varepsilon)$ shown in Figure 3a
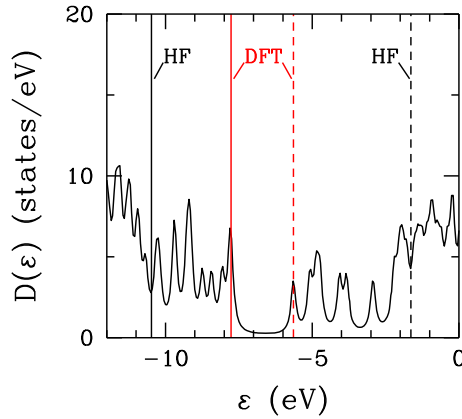
Fig. 16. DFT results on the total density of states $D(\varepsilon)$ of Im-[Co^{III}(corrin)]-CN$^+$ obtained by using the Gaussian program with the BP86 exchange correlation potentials and the 6-31G basis set. The solid and dashed vertical red lines denote the HOMO and LUMO levels obtained by the DFT calculation. Similarly, the solid and dashed vertical black lines denote the HOMO and LUMO levels obtained by the Hartree-Fock calculation described in Section 2. Here, we see that in the DFT calculations additional spectral weight is induced in the intervals -10.5 eV $\leq \varepsilon \leq -7.8$ eV and -5.7 eV $\leq \varepsilon \leq -1.8$ eV when compared with the HF results.

with the DFT results of Figure 16, we observe that the HF HOMO and LUMO levels located at -10.5 eV and -1.7 eV move to -7.8 eV and -5.6 eV, respectively. Hence, in comparison to the HF results, the DFT calculation yields additional spectral weight in the energy intervals -10.5 eV $\lesssim \varepsilon \lesssim -7.8$ eV and -5.6 eV $\lesssim \varepsilon \lesssim -1.7$ eV.

Next, we compare the DFT results on $D(\varepsilon)$, Figure 16, with the single-particle spectral weight deduced from the HF+QMC data on the total electron number $\langle n_T \rangle$ versus μ shown in Figure 8c for $U = 36$ eV. We observe that the locations of the HOMO and LUMO levels obtained by DFT and HF+QMC are comparable. In addition, the DFT result for the total number of the electrons in the Co$(3d_\nu)$ NAO states is 7.4, which is similar to the HF+QMC result seen in Figure 9. So, the DFT and the HF+QMC results for the energy gap and $\langle n_d \rangle$ are comparable to each other as well as to the the experimental results. However, we will see in the following that there are important differences between the DFT and HF+QMC results when the overall distribution of the single-particle spectral weight near the semiconductor gap edges is considered.

In the HF+QMC data presented in Section 3 for $U = 36$ eV, we have seen that new states are induced in the energy interval -10 eV $\lesssim \varepsilon \lesssim -8$ eV which originate mainly from the doubly-occupied Co $3d_{xz}$, $3d_{x^2-y^2}$ and $3d_{yz}$ orbitals. This is because $\tilde{\varepsilon}_{d\nu} + U$ for the Co t_{2g}-like orbitals corresponds to this energy interval. In the same interval, there also exist smaller amount of host states due to hybridization with the Co t_{2g}-like states. On the other hand, the states induced in the interval -5.5 eV $\lesssim \varepsilon \lesssim -2$ eV in the HF+QMC data originate from the Co $3d_{3z^2-r^2}$ and $3d_{xy}$ states. These states are similar in nature to the

impurity bound states found in the mean-field and QMC studies of the Haldane-Anderson model for the DMS materials [10–12]. We have also seen that host states, which are mainly originating from the CN axial ligand, are induced in the energy interval -5.5 eV $\lesssim \varepsilon \lesssim -2$ eV. In fact, here, the amount of the single-particle spectral weight originating from the host states is larger than that from the e_g-like states. From Figures 8a and 8b, we observe that in the interval -5.5 eV $\lesssim \varepsilon \lesssim -2$ eV the host states accommodate about 1.6 electrons while the e_g-like states accommodate about 0.4 electrons.

Now, we discuss the nature and origin of the states forming in the energy intervals -10 eV $\lesssim \varepsilon \lesssim -8$ eV and -5 eV $\lesssim \varepsilon \lesssim -2$ eV in the DFT calculations. For this purpose, we present DFT results in Table 1 on the NAO spectral weights of the molecular orbitals located in these intervals. Using the DFT data, we expand the one-electron molecular orbitals $|\psi_n\rangle$ in terms of the NAO's of the whole molecule including both the host and the Co $(3d)$ states,

$$|\psi_n\rangle = \sum_i^N \tilde{C}_{ni}|\tilde{\phi}_i\rangle. \tag{21}$$

Here, the sum over the NAO index i goes upto $N = 347$. Table 1 shows DFT results on $|\tilde{C}_{ni}|^2$ for the molecular orbitals which are located right below and above the DFT semiconductor gap. In particular, here results are shown for the molecular orbitals with index $109 \leq n \leq 130$, which includes the states located in the intervals -10.22 eV $\leq \varepsilon \leq -7.77$ eV and -5.64 eV $\leq \varepsilon \leq -1.78$ eV. We are interested in how much Co $(3d)$ NAO weight these molecular orbitals contain. We are also interested in how much NAO weight of the CN axial ligand is included in these energy intervals. We will compare them with the HF+QMC data. It is for these purposes that the data in Table 1 are presented.

The first and the second columns of Table 1 denote the location of a given molecular orbital with respect to the semiconductor gap and the molecular orbital index n. The third column shows the corresponding molecular energy E_n. The following five columns show $|\tilde{C}_{ni}|^2$ for the Co $(3d)$ NAO states. The last two columns show the NAO weights summed over the three $2p$ orbitals, $\sum_{2p} |\tilde{C}_{ni}|^2$, for the C and N atoms of the CN axial ligand. We note that the C and N atoms of the CN axial ligand are labelled as 30C and 31N following the notation of the Gaussian program [31].

Here, we observe that the molecular orbitals with the index $n = 115$ through 118 contain significant amount of spectral weight from the Co $3d_{xz}$, $3d_{x^2-y^2}$ and $3d_{yz}$ NAO's. In comparison, the HOMO state ($n = 119$) and the LUMO state ($n = 120$) contain smaller amount of Co $3d_{yz}$ NAO weight. On the other hand, the molecular orbitals $n = 121$ and 122 contain significant amount of Co $3d_{xy}$ and $3d_{3z^2-r^2}$ NAO weights, respectively.

Next, we compare these DFT results with the HF+QMC data from Section 3. In the DFT results, we see that in the interval -10 eV $\lesssim \varepsilon \lesssim -8$ eV there is spectral weight originating from the Co $3d_{x^2-y^2}$, $3d_{xz}$ and $3d_{yz}$

Table 1. DFT results on the NAO spectral weights $|\tilde{C}_{ni}|^2$ of the molecular orbitals near the semiconductor gap edges for Im-[Co$^{\mathrm{III}}$(corrin)]-CN$^+$. Here, n is the index for the molecular orbital, and i is for the NAO. The first two columns denote the molecular orbital and the corresponding index. The following five columns denote how much Co (3d) NAO spectral weight exists in the nth molecular orbital. Similarly, the last two columns denote the amount of the total 2p spectral weight at the C and N atoms in the CN axial ligand. For convenience, when $|\tilde{C}_{ni}|^2 \geq 0.05$, the numbers are printed in bold face.

| Molecular orbital | n | E_n (eV) | Co $(3d_\nu)$ | | | | | 30C | 31N |
			$3z^2-r^2$	xy	xz	x^2-y^2	yz	(summed over 2p's)	(summed over 2p's)
HOMO-10	109	-10.22	0.0	0.0	0.0	0.0	0.02	0.01	0.01
HOMO-9	110	-9.70	0.0	0.0	**0.10**	0.0	0.01	**0.14**	**0.14**
HOMO-8	111	-9.69	0.0	0.0	0.01	0.0	**0.16**	**0.25**	**0.24**
HOMO-7	112	-9.27	0.04	0.0	0.0	0.0	0.0	**0.09**	**0.49**
HOMO-6	113	-9.19	0.01	0.0	0.0	0.0	0.0	**0.14**	**0.28**
HOMO-5	114	-9.15	0.0	0.0	0.0	0.0	0.0	0.0	0.01
HOMO-4	115	-8.74	0.0	0.0	0.0	**0.08**	**0.15**	**0.09**	**0.21**
HOMO-3	116	-8.43	0.0	0.02	0.0	**0.83**	0.02	0.01	0.03
HOMO-2	117	-8.07	0.0	0.01	**0.66**	0.0	0.0	0.02	**0.12**
HOMO-1	118	-7.80	0.02	0.0	0.0	0.0	**0.38**	0.01	0.03
HOMO	119	-7.77	0.01	0.0	0.01	0.01	**0.10**	0.01	0.02
LUMO	120	-5.64	0.0	0.0	0.0	0.0	**0.05**	0.0	0.0
LUMO+1	121	-5.08	0.03	**0.49**	0.02	0.01	0.0	0.0	0.0
LUMO+2	122	-4.87	**0.38**	0.07	0.01	0.0	0.01	**0.06**	0.02
LUMO+3	123	-4.74	**0.09**	0.01	0.04	0.0	0.0	0.01	0.01
LUMO+4	124	-4.07	0.0	0.01	0.0	0.0	0.0	0.0	0.0
LUMO+5	125	-3.83	0.0	0.0	0.0	0.0	0.0	0.0	0.0
LUMO+6	126	-2.93	0.0	0.0	0.0	0.0	0.0	0.0	0.0
LUMO+7	127	-2.20	0.0	0.0	0.0	0.0	0.0	0.01	0.01
LUMO+8	128	-2.03	0.0	0.0	0.0	0.0	0.0	0.01	0.01
LUMO+9	129	-1.93	0.0	0.0	0.0	0.0	0.01	0.01	0.01
LUMO+10	130	-1.78	0.0	0.0	0.0	0.0	0.0	0.0	0.0

NAO states. This agrees with the HF+QMC data. However, the amounts of the single-particle spectral weight contained in this interval are different. According to the DFT results, in this interval the Co $3d_{xz}$, $3d_{x^2-y^2}$ and $3d_{yz}$ NAO's accommodate 1.56, 1.84 and 1.88 electrons, respectively, including spin. On the other hand, as seen in Figure 7a, the HF+QMC approach finds that each of these orbitals contains in this interval about 0.9 electrons including spin. In this case, the interval -10 eV $\lesssim \varepsilon \lesssim -8$ eV is approximately equal to the value of $\tilde{\varepsilon}_{d\nu} + U$. Hence, the states in this interval correspond mainly to the upper Hubbard states of the t_{2g}-like NAO's. This comparison shows that the DFT calculations do not yield the splitting of the t_{2g}-like states into the lower and upper Hubbard states found by HF+QMC.

Next, we discuss the DFT results for the interval -5 eV $\lesssim \varepsilon \lesssim -2$ eV, which contains spectral weight from the Co $3d_{xy}$ and $3d_{3z^2-r^2}$ NAO states. The HF+QMC data also finds spectral weight from the Co $3d_{xy}$ and $3d_{3z^2-r^2}$ NAO's in this interval. However, the amounts of the spectral weight contained in this interval are different. According to the DFT results, the Co $3d_{xy}$ and $3d_{3z^2-r^2}$ NAO's contain 1.16 and 1.0 electrons in this interval. The HF+QMC yields 0.2 electrons for each of these orbitals in the same interval.

In the last two columns of Table 1 on the DFT results, we observe that in the interval -5.5 eV $\lesssim \varepsilon \lesssim -2$ eV, there is little amount of NAO spectral weight originating from the CN axial ligand. In the HF+QMC data, however,

there is significant amount of spectral weight from the CN axial ligand in this energy interval. This is because the CN axial ligand hybridizes strongly with the Co $3d_{xy}$ and $3d_{x^2-y^2}$ NAO's. Hence, in the DFT calculations the states in the interval -5.5 eV $\lesssim \varepsilon \lesssim -2$ eV do not arise from an impurity bound state as found in the HF+QMC calculations.

When we compare the DFT and the HF+QMC results, we find good agreement for the magnitude of the HOMO-LUMO gap and the total occupation number $\langle n_d \rangle$ of the Co (3d) orbitals. However, there exist important differences in the overall distribution of the single-particle spectral weight near the semiconductor gap edges. In particular, we see that the DFT calculation yields much less spectral weight in the interval -5.6 eV $\lesssim \varepsilon \lesssim -1.8$ eV originating from the CN axial ligand. In addition, according to DFT, the Co $(3d_\nu)$ spectral weight in the interval -10 eV $\leq \varepsilon \leq -8$ eV does not arise from the split upper-Hubbard states of the Co t_{2g}-like orbitals.

Furthermore, in Table 1 we see that, in the interval -10.22 eV $\leq \varepsilon \leq -1.78$ eV, there are 22 molecular orbitals, which can accommodate a total of 44 electrons. On the other hand, in the HF+QMC data shown in Figure 8c, we observe that there is spectral weight to contain only 5 electrons in the interval -10 eV $\lesssim \varepsilon \lesssim -2$ eV. Hence, the single-particle spectrum in this interval is much denser according to the DFT results.

In addition to these, we have also performed DFT calculations by using the B3LYP exchange-correlation

functional [52,53] instead of the BP86. We do not present these results here because of the length of the manuscript. In this case, the energy gap is ≈3.2 eV. However, the distribution of the spectral weight near the HOMO and LUMO levels is similar to that shown in Table 1 for BP86.

Furthermore, we have also performed calculations by using the local spin density approximation [54] (LSDA) for Im-[Co^{III}(corrin)]-CN$^+$ with the Gaussian program [31]. In that case, the energy gap is ≈2.1 eV, and the overall distribution of the single-particle spectral weight is similar to the DFT results shown in Table 1. As in the DFT calculations, the LSDA approach does not capture the Hubbard splitting of the t_{2g}-like orbitals, and the states at the LUMO level do not arise from an impurity bound state.

In addition to metalloproteins and metalloenzymes, the DFT technique is widely applied for studying transition-metal-containing organometallic molecules, which are used in fields ranging from solar-cell applications to hydrogen storage. The differences discussed here between the DFT and the HF+QMC approaches might simply be due to the fact that the present HF+QMC approach is too simple to describe the electronic state of CNCbl. If that is not the case, then these comparisons suggest that caution is necessary in interpreting the results of the DFT technique when used for studying organometallic molecules containing transition metal atoms.

In addition to these, the DFT and HF+QMC results differ on the nature of the electronic correlations. The HF+QMC technique finds that antiferromagnetic correlations exist between the Co e_g magnetic moments and the electronic spins localized at the CN axial ligand depending on the filling of the impurity bound states. However, the magnetic correlations are not contained in the DFT results, as it is well-known.

4.2 Comparison of the HF+QMC data with the photoabsorption spectrum of CNCbl

The photoabsorption spectrum of CNCbl is characterized by several distinctive peaks [6]. The lowest-energy peak in the spectrum occurs at ≈2.25 eV and it is associated with the so-called S_1 electronically excited state of CNCbl. The largest peak, on the other hand, is located at ≈3.4 eV. There have been various DFT based studies [17,23–26] to identify the origin of the peaks in the spectra of the Cbl cofactors.

For a long time, the lowest-energy part of the photoabsorption spectrum of Cbl had been associated with a transition which is dominated by the $\pi \rightarrow \pi^*$ excitations of the corrin ring [1], which represent electronic transitions among the $2p\pi$ orbitals in the corrin ring. The reason for this assignment is that the metal-free corrinoids also exhibit a similar peak in the spectrum. The time-dependent DFT calculations with the BP86 functionals on the truncated molecule Im-[Co^{III}(corrin)]-CN$^+$ have supported the view that the S_1 state corresponds mainly to $\pi \rightarrow \pi^*$ transitions in the corrin ring [24]. On the other hand, the ultrafast transient absorption spectroscopy measurements

on CNCbl [55,56] have suggested a picture for the S_1 transition in which charge transfer from the π orbitals of the corrin ring to the Co atom takes place. In spite of these developments, today it is considered that much still remains to be understood about the nature of the excited states of Cbl cofactors. In particular, there is much interest to clarify the origin of the lowest excited S_1 state.

In order to compare the photoabsorption spectrum of CNCbl with the HF+QMC data on the electronic structure of Im-[Co^{III}(corrin)]-CN$^+$, we assume that the rigid band approximation can be used for describing the single-particle spectral weight distribution of the Haldane-Anderson model. According to the HF+QMC results shown in Figure 8 for $U = 36$ eV, when the chemical potential $\mu \approx -8.5$ eV, the truncated system Im-[Co^{III}(corrin)]-CN$^+$ has 238 electrons. In this case, the highest occupied states consist of the Co t_{2g}-like states which are the $3d_{xz}$, $3d_{x^2-y^2}$ and $3d_{yz}$ NAO's in our coordinate system. Smaller amount of weight from the $2p\pi$ orbitals of the corrin ring is also included. In the dominant lowest-energy photoabsorption process, an electron initially occupying a Co t_{2g}-like state would be transferred to the lowest excited state located at ≈−5.5 eV. We have seen in Section 3.3 that this state at ≈−5.5 eV corresponds to an impurity bound state and consists mainly of the $2p\pi$ NAO's at the CN axial ligand. The impurity bound state contains lesser amounts of spectral weight from the $2p\pi$ NAO's of the corrin ring as well as from the Co ($3d_{xy}$) NAO. Hence, according to HF+QMC, the lowest excited state in the absorption spectrum corresponds mainly to a transition involving the transfer of an electron from the Co t_{2g}-like states to the impurity bound state, which consists of states at the CN axial ligand, the corrin ring and a Co e_g NAO.

If the electron is excited to the second lowest energy of Im-[Co^{III}(corrin)]-CN$^+$, then the in-gap states located at ≈−4 eV would become occupied. This impurity bound state consists mainly of the $2p\sigma$ and $2s$ NAO's of the CN axial ligand. Smaller amounts of spectral weight from the $2p\sigma$ orbitals of the corrin ring and of the Co ($3d_{3z^2-r^2}$) NAO are also included. Hence, this electronic transition would be dominated by the transfer of an electron from the Co t_{2g}-like states to the second impurity bound state. The transitions to the ≈−5.5 eV and ≈−4 eV impurity bound states would be the main features of the photoabsorption spectrum expected for Im-[Co^{III}(corrin)]-CN$^+$ according to the HF+QMC data for the Haldane-Anderson model.

In summary, according to the HF+QMC calculations the lowest-energy excitations are dominated by electron transfer from the Co t_{2g}-like states to the CN axial ligand. Now, the HF+QMC approach might be too simple to correctly deduce the excitation spectrum of vitamin B$_{12}$. Nevertheless, the HF+QMC results presented here suggest that it would be useful to look for signatures of a possible $3d \rightarrow$ CN ligand electron transfer process in the excitation spectrum of CNCbl. According to the HF+QMC calculations, such $3d \rightarrow$ CN ligand transitions would be accompanied by the vanishing of the antiferromagnetic correlations between the Co e_g and the CN ligand NAO's along with

the collapse of the magnetic moments at the CN ligand. In addition, when an electron is removed from t_{2g}-like orbitals, a magnetic moment would develop due to the lifting of the double occupancy in these orbitals. Hence, the $3d \rightarrow$CN ligand electron transfer would be accompanied by the magnetic moment transfer in the reverse direction from the CN ligand to the Co t_{2g} orbitals. It would be useful to probe experimentally these magnetic correlations predicted by HF+QMC. In particular, it would be interesting to see how the many-body effects discussed here would influence the magnetic circular dichroism spectrum of CNCbl [57].

4.3 DFT+QMC approach

An alternative method for studying the electronic structure and correlations of organometallic molecules such as Cbl is the DFT+QMC approach. There are various differences between the HF+QMC and DFT+QMC approaches. For example, in HF+QMC the correlations of the s and p orbitals in the molecules are treated at the HF level rather than the more accurate DFT. In addition, in HF+QMC a bare unscreened Coulomb interaction is used in the QMC part. The bare Coulomb repulsion has a value of order 36 eV when evaluated in the basis of the atomic orbitals with the 6-31G Gaussian functions. In the DFT+QMC, the QMC part of the calculations are performed by using a renormalized Coulomb interaction, which is usually of order 4 eV. This renormalization is due to screening by the s and p electrons in the system, and the renormalized Coulomb interaction can be obtained by the constrained local-density approximation [34,58,59]. It is important to note that in both approaches the choices used for the Coulomb interaction and the double-counting μ_{DC} represent different levels of approximations [41]. Hence, it would be useful to compare them.

A transition-metal atom placed in an organic molecule, as in Cbl, is one of the simplest strongly-interacting systems. With the availability of spectroscopic data, this is a case where the combined electronic-structure and many-body approaches can be tested. In this respect, a thorough comparison of the HF+QMC and DFT+QMC approaches would be useful. Because of manuscript length considerations, this will be presented elsewhere [60].

4.4 Inter-orbital Coulomb interaction and the Hund's coupling

In this paper, we have presented HF+QMC results, where we used a constant U for the intra-orbital Coulomb interaction in the QMC part. It is well-known that the inter-orbital Coulomb interaction is important in the cobaltates [28]. Here, the inter-orbital Coulomb interactions are taken into account only at the Hartree-Fock level. A more accurate approach would be to include the inter-orbital Coulomb interaction in the QMC calculations. This can be done by replacing the last term in equation (1) by

$$\frac{1}{2}\sum_{\nu,\nu'}\sum_{\sigma} U_{\nu\nu'} n_{\nu\sigma} n_{\nu',-\sigma} + \frac{1}{2}\sum_{\nu \neq \nu'}\sum_{\sigma}(U_{\nu\nu'} - J_{\nu\nu'}) n_{\nu\sigma} n_{\nu'\sigma},$$

(22)

where $U_{\nu\nu'}$ and $J_{\nu\nu'}$ are the Coulomb matrix elements for the direct and the Hund's exchange couplings. For consistency, it is necessary to evaluate the Coulomb matrix elements in the NAO basis, since the one-electron parameters of the Anderson Hamiltonian are obtained by using the NAO's.

The interaction, equation (22), includes only density-density terms, hence it can be implemented in the Hirsch-Fye QMC algorithm. This improvement would still neglect the pair-hopping and the spin-flip terms of the Hund's coupling, which have been shown to be important in transition-metal oxides [61,62]. The double-counting correction μ_{DC} would also need to be re-evaluated after including the inter-orbital Coulomb interactions [45–47].

We think that it is necessary to include the inter-orbital Coulomb interaction before performing quantitative comparisons with the experimental data on the Cbl cofactors. The Hund's coupling may influence the magnetic correlations and cause additional splitting of the energy levels. After these improvements, the spin state of Co can be determined. In addition, the uniform magnetic susceptibility for electronic spins can be calculated to extract the effective magnetic moment for the molecule.

5 Summary and conclusions

In summary, we have studied the electronic structure and correlations of CNCbl from the perspective of the many-body physics. For this purpose, we have used the framework of the multi-orbital single-impurity Haldane-Anderson model of a transition-metal impurity placed in a semiconductor host. First, we have constructed an effective Haldane-Anderson model by using the HF approximation. In particular, we determined the one-electron parameters of the Anderson Hamiltonian from the Fock matrix written in the basis of the natural atomic orbitals by using HF. The double-counting of the Coulomb interaction within HF+QMC was taken into account by a chemical shift μ_{DC} of the Co $(3d_{\nu})$ levels. We used an orbital independent intra-orbital Coulomb interaction U in the QMC calculations neglecting the inter-orbital terms. We presented QMC results for various values U. However, we concentrated on the case $U = 36$ eV, since this yields values for the HOMO-LUMO gap and the total Co $(3d)$ electron number which are comparable to the experimental data.

The QMC data on this effective model showed how the energy gap found in the HF approximation is reduced by the generation of new in-gap states. The correlated nature of the induced states is clearly seen. In particular, states arising from the double-occupancy of the Co t_{2g} orbitals are induced near the gap edge above the HOMO level from HF, where as impurity bound states are induced below the LUMO level. The impurity bound states

arise from the strong hybridization of the Co e_g orbitals with the host eigenstates and contain significant amount of weight from the CN axial ligand and the corrin ring. We have also seen that magnetic moments can develop at the CN axial ligand and in the corrin ring, which are antiferromagnetically correlated with the Co e_g moments. These disappear rapidly with electron filling of the impurity bound states.

We have also presented a comparison of the HF+QMC data with the DFT calculations on Im-[Co^{III}(corrin)]-CN$^+$. While these two approaches yield similar values for the HOMO-LUMO gap and the total Co$(3d)$ occupation number, the results on the distribution of the single-particle spectral weights can be very different. In particular, the Hubbard-type splitting of the Co$(3d_\nu)$ states, the impurity bound states and the magnetic correlations are not contained in the DFT results. We have also presented the predictions of HF+QMC for the photoabsorption spectrum according to which the lowest-energy photoabsorption excitations are dominated by electron transfer from the Co t_{2g} orbitals to the impurity bound states.

It will be interesting to perform similar calculations for AdoCbl and MeCbl and compare their results with the results presented here on CNCbl. In particular, it would be useful to see whether it is possible to understand the catalytic functioning of these Cbl cofactors by using the HF+QMC calculations. It would also be useful to use the same framework to study hemoglobin containing Fe.

It is worth noting that the Co-C bond in Cbl is the first case of a metal-carbon bond to be found in biology. All of the known reactions of the Cbl-dependent enzymes involve the making and breaking of the Co-C bond [2]. In this respect, it is interesting that the impurity bound state contains significant amount of spectral weight from the CN axial ligand attached to Co. It would also be interesting to see whether the impurity bound state plays a role in the important Co-C bonding. If the making and breaking of the Co-C bond somehow involves the magnetic correlations around the Co atom, then this could be a way such that the occupancy of the impurity bound state becomes important.

The present HF+QMC approach contains various approximations. For instance, the inter-orbital Coulomb interaction is not treated by QMC, instead it is included at the Hartree-Fock level. In addition, the bare Coulomb repulsion U and the double-counting μ_{DC} are used more as variables than as true ab initio parameters. The geometrical parameters for the molecular structure are simple estimates since the actual atomic coordinates for CNCbl are not known. In spite of these, the HF+QMC yields reasonable values for the HOMO-LUMO gap and the total Co$(3d)$ occupation number, and interesting results for the photoabsorption spectrum. In particular, the HF+QMC results emphasize the many-body effects such as the Hubbard splitting of the Co$(3d_\nu)$ states and the possible existence of impurity bound states and magnetic correlations.

In conclusion, according to the HF+QMC results presented here, there is a possibility that an impurity bound state exists in the electronic spectrum of CNCbl. We think that it is necessary to seek further experimental evidence for this prediction of the HF+QMC calculations.

Authors contribution statement

All authors contributed equally to this paper.

References

1. J.M. Pratt, *Inorganic Chemistry of Vitamin B₁₂* (Academic Press, 1972)
2. B. Krautler, D. Arigoni, B.T. Golding, *Vitamin B₁₂ and B₁₂ proteins* (Wiley, 1998)
3. *Chemistry and Biochemistry of B₁₂*, edited by R. Banerjee (Wiley, 1999)
4. K.L. Brown, Chem. Rev. **105**, 2075 (2005)
5. D.C. Hodgkin, J. Kamper, M. Mackay, J.W. Pickworth, K.N. Trueblood, J.G. White, Nature **178**, 64 (1956)
6. A. Firth, H.A.O. Hill, J.M. Pratt, R.J.P. Williams, W.R. Jackson, Biochemistry **6**, 2178 (1967)
7. H. Ohno, H. Munekata, T. Penney, S. von Molnar, L.L. Chang, Phys. Rev. Lett. **68**, 2664 (1992)
8. H. Ohno, A. Shen, F. Matsukura, A. Oiwa, A. End, S. Katsumoto, Y. Iye, Appl. Phys. Lett. **69**, 363 (1996)
9. T. Jungwirth, J. Sinova, A.H. MacDonald, B.L. Gallagher, V. Novak, K.W. Edmonds, A.W. Rushforth, R.P. Campion, C.T. Foxon, L. Eaves, E. Olejnik, J. Masek, S.-R. Eric Yang, J. Wunderlich, C. Gould, L.W. Molenkamp, T. Dietl, H. Ohno, Phys. Rev. B **76**, 125206 (2007)
10. M. Ichimura, K. Tanikawa, S. Takahashi, G. Baskaran, S. Maekawa, in *Foundations of Quantum Mechanics in the Light of New Technology*, edited by S. Ishioka, K. Fujikawa (World Scientific, 2006)
11. N. Bulut, K. Tanikawa, S. Takahashi, S. Maekawa, Phys. Rev. B **76**, 045220 (2007)
12. Y. Tomoda, N. Bulut, S. Maekawa, Physica B **404**, 1159 (2009)
13. F.D.M. Haldane, P.W. Anderson, Phys. Rev. B **13**, 2553 (1976)
14. P.W. Anderson, Phys. Rev. **124**, 1 (1961)
15. J.E. Hirsch, R.M. Fye, Phys. Rev. Lett. **56**, 2521 (1986)
16. K.P. Jensen, S.P.A. Sauer, T. Liljefors, P. Norrby, Organometallics **20**, 550 (2001)
17. T. Andruniow, P.M. Kozlowski, M.Z. Zgierski, J. Chem. Phys. **115**, 16 (2001)
18. L. Ouyang, L. Randaccio, P. Rulis, E.Z. Kurmaev, A. Moewes, W.Y. Ching, J. Mol. Struct. (Theochem) **622**, 221 (2003)

19. E.Z. Kurmaev, A. Moewes, L. Ouyang, L. Randaccio, P. Rulis, W.Y. Ching, M. Bach, M. Neumann, Europhys. Lett. **62**, 582 (2003)
20. L. Ouyang, P. Rulis, W.Y. Ching, G. Nardin, L. Randaccio, Inorg. Chem. **43**, 1235 (2004)
21. C. Rovira, P.M. Kozlowski, J. Phys. Chem. B **111**, 3251 (2007)
22. S. Mebs, J. Henn, B. Dittrich, C. Paulmann, P. Luger, J. Phys. Chem. A **113**, 8366 (2009)
23. H Solheim, K. Kornobis, K. Ruud, P.M. Kozlowski, J. Phys. Chem. B **115**, 737 (2011)
24. K. Kornobis, N. Kumar, B.M. Wong, P. Lodowski, M. Jaworska, T. Andruniow, K. Ruud, P.M. Kozlowski, J. Phys. Chem. A **115**, 1280 (2011)
25. A.J. Reig, K.S. Conrad, T.C. Brunold, Inorg. Chem. **51**, 2867 (2012)
26. K. Kornobis, N. Kumar, P. Lodowski, M. Jaworska, P. Piecuch, J.J. Lutz, B.M. Wong, P.M. Kozlowski, J. Comp. Chem. **34**, 987 (2013)
27. H. Chen, M. Ikeda-Saito, S. Shaik, J. Am. Chem. Soc. **130**, 14778 (2008)
28. S. Maekawa, T. Tohyama, S.E. Barnes, S. Ishihara, W. Koshibae, G. Khaliullin, *Physics of Transition Metal Oxides* (Springer, 2004)
29. K. Yamauchi, H. Maebashi, H. Katayama-Yoshida, J. Phys. Soc. Jpn **72**, 2029 (2003)
30. V. Badaut, T. Shirakawa, S. Yunoki, J. Phys.: Conf. Ser. **400**, 032006 (2012)
31. M.J. Frisch, G.W. Trucks, H.B. Schlegel, G.E. Scuseria, M.A. Robb, J.R. Cheeseman, G. Scalmani, V. Barone, B. Mennucci, G.A. Petersson, H. Nakatsuji, M. Caricato, X. Li, H.P. Hratchian, A.F. Izmaylov, J. Bloino, G. Zheng, J.L. Sonnenberg, M. Hada, M. Ehara, K. Toyota, R. Fukuda, J. Hasegawa, M. Ishida, T. Nakajima, Y. Honda, O. Kitao, H. Nakai, T. Vreven, J.A. Montgomery, Jr., J.E. Peralta, F. Ogliaro, M. Bearpark, J.J. Heyd, E. Brothers, K.N. Kudin, V.N. Staroverov, R. Kobayashi, J. Normand, K. Raghavachari, A. Rendell, J.C. Burant, S.S. Iyengar, J. Tomasi, M. Cossi, N. Rega, J.M. Millam, M. Klene, J.E. Knox, J.B. Cross, V. Bakken, C. Adamo, J. Jaramillo, R. Gomperts, R.E. Stratmann, O. Yazyev, A.J. Austin, R. Cammi, C. Pomelli, J.W. Ochterski, R.L. Martin, K. Morokuma, V.G. Zakrzewski, G.A. Voth, P. Salvador, J.J. Dannenberg, S. Dapprich, A.D. Daniels, O. Farkas, J.B. Foresman, J.V. Ortiz, J. Cioslowski, D.J. Fox, *Gaussian 09*, Revision D.01 (Gaussian, Inc., Wallingford CT, 2009)
32. A.E. Reed, L.A. Curtis, F. Weinhold, Chem. Rev. **88**, 899 (1988)
33. E.D. Glendening, J.K. Badenhoop, A.E. Reed, J.E. Carpenter, J.A. Bohmann, C.M. Morales, C.R. Landis, F. Weinhold, NBO 6.0, Theoretical Chemistry Institute, University of Wisconsin, Madison, 2013
34. O. Gunnarsson, O.K. Andersen, O. Jepsen, J. Zaanen, Phys. Rev. B **39**, 1708 (1989)
35. Z. Kandemir, Master's Thesis, Izmir Institute of Technology, 2013
36. L. Randaccio, M. Furlan, S. Geremia, M. Slouf, I. Srnova, D. Toffoli, Inorg. Chem. **39**, 3403 (2000)
37. A.D. Becke, Phys. Rev. A **38**, 3098 (1988)
38. J.P. Perdew, Phys. Rev. B **33**, 8822 (1986)
39. J.C. Slater, Phys. Rev. **81**, 385 (1951)
40. F. Jensen, *Introduction to Computational Chemistry* (John Wiley, 2007)
41. K. Held, Adv. Phys. **56**, 829 (2007)
42. N. Marzari, D. Vanderbilt, Phys. Rev. B **56**, 12847 (1997)
43. I. Schnell, G. Czycholl, R.C. Albers, Phys. Rev. B **65**, 075103 (2002)
44. I. Schnell, G. Czycholl, R.C. Albers, Phys. Rev. B **68**, 245102 (2003)
45. V.I. Anisimov, J. Zaanen, O.K. Andersen, Phys. Rev. B **44**, 943 (1991)
46. M.T. Czyzyk, G.A. Sawatzky, Phys. Rev. B **49**, 14211 (1994)
47. J. Kuneš, V.I. Anisimov, A.V. Lukoyanov, D. Vollhardt, Phys. Rev. B **75**, 165115 (2007)
48. M. Karolak, G. Ulm, T.O. Wehling, V. Mazurenko, A. Poteryaev, A.I. Lichtenstein, J. Electron. Spectrosc. Relat. Phenomena **181**, 11 (2010)
49. S. Mayda, Master's Thesis, Izmir Institute of Technology, 2013
50. F. Grun, R. Menasse, Experientia **6**, 263 (1950)
51. H. Diehl, R.W.V. Haar, R.R. Sealock, J. Am. Chem. Soc. **72**, 5312 (1950)
52. A.D. Becke, J. Chem. Phys. **98**, 5648 (1993)
53. C. Lee, W. Yang, R.G. Parr, Phys. Rev. B **37**, 785 (1988)
54. S.H. Vosko, L. Wilk, M. Nusair, Can. J. Phys. **58**, 1200 (1980)
55. J.J. Shiang, A.G. Cole, R.J. Sension, K. Hang, Y. Weng, J.S. Trommel, L.G. Marzilli, T. Lian, J. Am. Chem. Soc. **128**, 801 (2006)
56. D.A. Harris, A.B. Stickrath, E.C. Carroll, R.J. Sension, J. Am. Chem. Soc. **129**, 7578 (2007)
57. T.A. Stich, A.J. Brooks, N.R. Buan, T.C. Brunold, J. Am. Chem. Soc. **125**, 5897 (2003)
58. P.H. Dederichs, S. Blügel, R. Zeller, H. Akai, Phys. Rev. Lett. **53**, 2512 (1984)
59. A.K. McMahan, R.M. Martin, S. Satpathy, Phys. Rev. B **38**, 6650 (1988)
60. S.M. Bacaksiz, Z. Kandemir, N. Bulut (unpublished)
61. S. Sakai, R. Arita, K. Held, H. Aoki, Phys. Rev. B **74**, 155102 (2006)
62. A.S. Belozerov, I. Leonov, V.I. Anisimov, Phys. Rev. B **87** 125138 (2013)